Title
Theoretical aspects of chalcogen-based semiconductor thin films manufacturing

Author
Batiz Guerrero, Humberto

Publication Date
2022

Peer reviewed|Thesis/dissertation

Theoretical aspects of chalcogen-based semiconductor thin films manufacturing

by

Humberto Batiz Guerrero

A dissertation submitted in partial satisfaction of the

requirements for the degree of

Doctor of Philosophy

in

Engineering- Materials Science & Engineering

in the

Graduate Division

of the

University of California, Berkeley

Committee in charge:

Professor Daryl C. Chrzan, Chair
Professor Ali Javey
Professor Mark Asta

Fall 2022

Theoretical aspects of chalcogen-based semiconductor thin films manufacturing

Abstract

Theoretical aspects of chalcogen-based semiconductor thin films manufacturing

by

Humberto Batiz Guerrero

Doctor of Philosophy in Engineering- Materials Science & Engineering

University of California, Berkeley

Professor Daryl C. Chrzan, Chair

Chalcogen-based materials, specially those containing S, Se or Te, can can be successfully manufactured into thin films with semiconducting properties. Transition metal dichalcogenides (TMDCs) are a class of layered materials whose electronic properties are known to depend on the elastic state. Mono- and bi-layer WSe_2, for example, undergoes a strain-induced direct to indirect band gap transition. This feature, in principle, could be of great use to design single-material electronic devices were circuits are "drawn" in different elastic states. While it is possible to grow TMDCs in a variety of elastic states, precise control of local strain is yet to be achieved. The first part of this dissertation develops a theoretical model for an empirically-tested method of strain release for TMDCs with built-in strain: the solvent evaporation-mediated decoupling (SEMD) method. The purpose of building such model is to generate knowledge about the underlying mechanism that allows the strain release, and once this process is better understood, to propose further generalizations and experiments that could lead to a better engineering of the elastic states.

The SEMD process consists simply in letting a droplet of liquid solvent evaporate on top of a strained layer. The process was first reported in WSe_2 monolayers grown by physical vapor deposition (PVD) on top of amorphous silica; in this case, as the system cooled down from growth to room temperature, strain build up in the film due to the mismatch between its thermal expansion coefficient and that of the substrate. By finding the elastic equilibrium state of a Hamiltonian that takes into account the elastic, interfacial, and substrate-film interaction energies, the proposed model finds an in-plane deformation beyond the film's initial strain as the main effect of the solvent droplet, and identifies it as the strain release mechanism. Furthermore, the proposes a selectivity criteria based on the contact angle that determines whether the SEMD process would be successful for a given initial elastic state.

The second part of the thesis is about thin films made of Te. Te-based materials were heavily studied in the 1980's due to their applications in data storage, and are now experiencing a revival mainly because its potential application in electronic and optic devices. Due to

the chain-like nature of the crystalline Te structure, this material's properties are highly anisotropic, with the conductivity, for example, being greater in the direction parallel to the chains. Because of this anisotropy, high-quality devices require large areas of single-crystalline Te.

Here, we explore the crystallization process of vapor-grown amorphous Te under different temperatures and, using tools from classical nucleation theory, investigate the nucleation and growth rate of crystals in an amorphous matrix. As a low nucleation rate will necessarily result in slow growth, another mechanism to grow Te single crystals is needed. An alternative route is offered by growing Te upon WTe_2, a substrate with two-fold symmetry that favors chain alignment along its high-symmetry direction. Crystals nucleating on top of WTe_2 are found to have single crystal-like texture, and thus be suitable for device applications.

A Humberto, Maru, Ana Isabel y Ana Paula: mi familia
A los demás

Contents

Contents **ii**

List of Figures **iii**

List of Tables **vi**

1 Introduction **1**

2 Solvent-Evaporation Mediated Decoupling **3**
2.1 Experimental details 3
2.2 Calculus of Variations 4
2.3 Model overview 7
2.4 Results and discussion 19
2.5 Conclusion 22

3 Tellurium crystalline thin film growth **24**
3.1 Experimental details 25
3.2 Nucleation and growth phenomena 25
3.3 Image analysis 28
3.4 Results and discussion 32
3.5 Conclusions 33

4 Oriented growth of thin Te crystals **36**
4.1 Results and discussion 36
4.2 Conclusions 41

5 Conclusions and future work **42**

Bibliography **44**

List of Figures

2.1 A schematic of the continuum model: (a) side view and (b) top-down view. The WSe_2 sample is assumed to be circular in shape with unstrained radius R, and rigidly attached to the substrate within the radius Δ, again defined in the unstrained material coordinate system. The material within this radius is assumed to be under the fixed biaxial strain ε_0 (that arises from the synthesis process). The radius of the contact patch between the acetone and the film is taken to be r_0, also in the unstrained material coordinate system. The contact angle θ also is shown. 8

2.2 (a) The generalized force on the decoupling boundary plotted as a function of Δ. (b) An estimate of the average force per atom experienced by atoms with $\Delta - \delta \leq r \leq \Delta$ computed as described in the text plotted vs. Δ for three different values of δ. The magnitudes of these forces are approximately two orders of magnitude below the range associated with covalent bonding. 13

2.3 Energy of WSe_2/SiO_2 system as a function of the film-substrate separation, d. The solid line is Eqn. (2.49) using $D_e = 0.50\,\text{meV}\,\text{Å}^{-2}$ and $\beta = 1.31\,\text{Å}^{-1}$ 18

2.4 Energy differences of systems with and without OOPD. The parameters used where those shown in Table 2.1, $V = 150\,\mu\text{m}^3$, $\Delta = 5\,\mu\text{m}$. The values for r_0 and u_0 were obtained using the formalism shown in Sec. 2.3.2.1 20

2.5 In-plane displacement in the equilibrium configuration for a system with $\Delta = 5\,\mu\text{m}$ and different liquid volumes. The vertical black line corresponds to $r = \Delta$, while the others correspond to $r = r_0$ for the different values of V 21

2.6 Percentage increase in decoupling force (now elastic plus droplet effects) relative to just the elastic force for three different droplet volumes plotted as a function of Δ. The step discontinuity at larger Δ arises from the fact that, within the model, there is no extra force if the radius of the pinned region is larger than the radius of the droplet contact patch. 22

2.7 Schematics, displacement and strains for a droplet on top of a strained film. For cases 3 and 4, a volume of $V = 500\,\mu m^3$ was used; $\gamma_{lv} = 0.45\,MeV^2\,\mu m^{-1}$ and $\gamma_{sl} = 0.40\,MeV^2\,\mu m^{-1}$ were selected so that γ_{lv} would match that of water and the Young's angle, defined by Eqn. (2.31), was 110°. Cases 2 and 4 use an initial strain of $\varepsilon_o = -0.7\%$. The white arrows indicate the direction of the displacements associated with the strain. For cases 1 and 4, the droplet has the potential to initiate decoupling of the film from the substrate. For cases 2 and 3, the droplet will likely stabilize the strain state. 23

3.1 Crystal structure of Te. 24
3.2 Transformed fraction for the sample held at 10 °C computed used the three methods with the same reference images. 30
3.3 a) Polarized optical microscopy of a sample after the crystallization was completed holding the sample at 15 °C. b) Processed version of (a). The image segmentation was done using the statistical region merging algorithm [1] using 25 random variable per pixel. Region colors were assigned just to facilitate differentiation. . 30
3.4 Grain density obtained by segmenting the micrographs of Te samples crystallized at different temperatures. Error bars were set to $0.02\,\mu m^{-2}$ to account for errors in the digitization of the data. 31
3.5 a) Binarized image of a grain and its fitted ellipse. b) Growth rate of the major and minor axis of the fitted ellipses for different temperatures. Error bars were obtained as the standard deviation of at least 3 tracked crystals. 31
3.6 The kinetic growth data obtained from analysis of experimental data for (i)...(vii) = 35, 30, 25, 20, 15, and 10°C, respectively. The solid red curves are the experimental data obtained from the digitized movies, and the black dashed curves represent the fits of the data to Eqn. 3.9. 32
3.7 Growth and nucleation rates determined by the fitting of Eqn. (3.9) and final grain number densities. All lengths are measured in microns, and times in seconds. 33
3.8 Temperature time transformation diagram for Te films crystallized at different temperatures. 5% and 95% means the coverage of the crystallized Te extracted from Fig. 3.6 34
3.9 Plot of growth rate as function of temperature, measured in $\mu m\,s^{-1}$. The solid line represents the fit to an Arrhenius equation. 35

4.1 Optical (a) and SEM (b) images of the oriented ultrathin Te on WSe_2 substrate. 37
4.2 Morphology of Te grown on WSe_2 under different conditions. a–c) Te grown at 100 °C on the non-annealed (a), 200 °C (b) and 300 °C (c) annealed WSe_2 substrates. d–f) Te grown at temperatures of 170 °C (d), 130 °C (e) and 100 °C (f) on the 300 °C pre-annealed WSe_2 substrates. 38

4.3 Kinetic Processes Affecting Morphology. a) Atoms arrive at the surface from the vapor. b) Atoms diffuse on the surface and c) may desorb from the surface, if they do not encounter a trapping site. d) Existing nuclei can serve as a trapping site. Once an atom encounters a wire, it is loosely bound and diffuses along the edge of the wire rapidly until it encounters the end of the wire, where it covalently bonds to the chain. e) Other atoms may also serve as trapping sites, leading, through standard nucleation kinetics, to homogeneous nucleation. f) Pre-existing defects can also serve as trapping sites, and can lead to heterogeneous nucleation. (Here the defect is a substitutional impurity atom.) g) After growth has progressed for some time, atoms will attach directly to nucleated clusters, and multilayer growth can ensue. 39

List of Tables

2.1 Numerical values of the material properties and the methods by which they were obtained. DFPT stands for Density Functional Perturbation Theory, and γ_{sl} was computed using Eqn. (2.31) with $\theta = 22°$. Values are in MeV $\mathring{A}^{-1}$ units. 12

3.1 Values of different system properties obtained using different methods to extract data from the videos. The process to calculate these properties is explained in Sec. 3.4 29

Acknowledgments

While on my PhD, I lost my father, my grandfather, two dogs and one cat, all this while a pandemic was upending every aspect of life. I didn't say this to have the reader's pity, but rather to to convince them of the amount of help I got along the way. Because, obviously, I couldn't have finished this thesis all by myself (not even in ideal conditions).

First, I would like to thank my family. My mother and father helped me in every way they could, and their love kept me going. Ana Isabel is everything I could ask for. Ana Paula is the backbone of the family. My extended family is big and I won't be naming them, but I also thank them and love them dearly.

My PhD experience would have been incomplete without the friends I made along the way. Your support is greatly appreciated.

My colleagues in Profs. Scott's and Javey's groups were essential to me. Thank you for trusting me with your experimental results and for being patient with me when I was developing my communication skills.

Lastly, I thank Prof. Chrzan and all the members of his group. The collaborative environment, the stimulating talks and the creative freedom are what every student needs to be successful in their PhD, and I was able to find it in this group. Keep up the good work!

Chapter 1

Introduction

A chalcogen is simply an element from group 16 of the periodic table. Group 16 comprises O, S, Te, Se, and Po. However, since O has a distinctive chemical nature and Po is radioactive and scarce, this thesis will focus on semiconductor compounds with S, Te, and Se. The chalcogenide compounds we will study will fall into two categories: transition metal dichalcogenides (TMDCs) and tellurium thin films.

TMDCs are layered materials whose fascinating properties [2, 3] make them candidates for electronic and optoelectronic applications. Accordingly, they have drawn attention from the research community. Both theoretical and experimental works have proved that their optical and electronic properties are a function both of their thickness and their elastic state [4–6]. It has been proved that mono- and bi-layer WSe_2, for example, undergoes a strain-induced direct to indirect band gap transition, drastically changing their photoluminescence[7]. Even though it is possible to induce uniform uni- and biaxial strain in TMDCs by means of substrate bending and stretching, and thermal expansion coefficient mismatch between the substrate and the film[4, 8], a method to locally control the strain state of TMDCs is still lacking. With the aid of such method, we could engineer the dependency of the optoelectronic properties on the elastic state. A precise control on the elastic state, and hence on the optoelectronic properties, may help to synthesize single-material electronic devices, with circuits following the lines of relaxed material.

A promising candidate for local strain control is the solvent-evaporation mediated decoupling (SEMD) method, reported experimentally in [9]. The SEMD process, presented in Chapter 2, consists in letting a droplet of liquid solvent evaporate on top of a strained layer. The process was first reported in WSe_2 monolayers grown by physical vapor deposition (PVD) on top of amorphous silica. According to the Ref. [9], the WSe_2 had an intrinsic tensile strain of $1.54 \pm 0.05\%$ due to a the mismatch in the thermal coefficients of expansion between the film and the substrate. Thus, with the objective of providing a better understanding of the SEMD process, the first part of this dissertation develops a theoretical model for the SEMD method. The model takes into account the elastic, interfacial, and substrate-film interaction energies, and identifies the critical parameters of the phenomenon. Moreover, by finding the equilibrium state of the proposed Hamiltonian, it is established that

the presence of the droplet deforms the film beyond the initial strain (it is also established that the film's out-of-plane deformation is negligible); this deformation, depending on the contact angle of the droplet and the sign of the initial strain, can trigger a strain relaxation event or stabilize the initial strain. The model, then, proposes a selectivity criteria based on the contact angle that determines whether the SEMD process would be successful for a given initial elastic state. With this selectivity criteria in mind, further experiments could be conducted to test the applicability of the model.

The second part of the thesis, chapters 3 and 4, is devoted to tellurium thin films. Te-based materials were heavily studied in the 1980's due to their applications in data storage, and are now experiencing a revival mainly because its potential application in electronic and optic devices. Te has a crystalline form composed of triangular chains, with the chains arranged hexagonally. While it is clear that the intra-chain bonds are covalent, the nature of the inter-chain bonds is yet to be established, but they are weaker than their intra-chain counterparts. The chain-like nature of the crystal structure results in the material properties being highly anisotropic, with the conductivity, for example, being greater in the direction parallel to the chains. Because of this anisotropy, high-quality devices require large areas of single-crystalline Te.

In chapter 3, the crystallization process of vapor-grown amorphous Te under different temperatures is explored. Analyzing experimentally-obtained polarized-light micrographs and in-situ videos of the crystallization process, it was possible to extract the growth and nucleation rate of crystalline nuclei within the initial amorphous matrix, as well as the final crystal number density for different experimental conditions. Later, using tools from classical nucleation theory, the nucleation and growth rates were related to growth and nucleation energy barriers. While it is proven that classical nucleation theory can be used to model the crystallization process in Te thin films, as a low nucleation rate will necessarily result in slow growth, no satisfactory way of producing large single crystals quickly is found.

Chapter 4 offers an alternative route to create large single-crystal-textured Te thin films: orienting the chains of multiple crystals in the same direction. This is achieved by growing Te in WTe_2, a substrate with two-fold symmetry that favors chain alignment along its two-fold axis. Crystals nucleating on top of WTe_2 are found to have single crystal-like texture, and thus be suitable for device applications. Also, this chapter offers theoretical insight about the kinetics of the growth and substrate treatments that increase the impingement rate of Te.

Each these chapters start with a brief motivation of the problem and a description of the experiment that is going to be modeled. Later, the theoretical tools are introduced and then the model is built. Finally, each chapter offers conclusions summarizing the results and proposing future theoretical work and further experiments.

Finally, Chapter 5 presents conclusions and proposes future work.

Chapter 2

Solvent-Evaporation Mediated Decoupling

Two-dimensional transition metal dichalcogenides (2D TMDCs) have been researched intensely due to their fascinating properties [2, 3]. Moreover, it has been proven that their optical and electronic properties can be strain engineered [4–6]. Accordingly, the need for a method by which the strain in 2D materials can be controlled has become more pressing. A promising candidate for engineering the strain is the solvent-evaporation mediated decoupling (SEMD) method that was first reported experimentally in [9].

This chapter is devoted to the presentation of the SEMD and a theoretical model that was developed to further explore SEMD method's capabilities and suggest new experiments. In section 2.1, we present a detailed account of the experiments in which SEMD was first observed. Section 2.2 introduces to the tools we are going to be using from the calculus of variations; the goal of this section is not to be a comprehensive treatise of the matter at hand, but rather a presentation of the equations used in the following. The theoretical model is developed in section 2.3, with subsections that go from the simplest case, that of a strained film on top of a substrate, to the most complex, when the a droplet on top of the film is considered and the film is allowed to have out-of-plane movement. Finally, results and conclusions are presented in sections 2.4 and 2.5, respectively. This chapter expands and borrows from what is said in Ref. [10].

2.1 Experimental details

Recently, it was shown that WSe_2 monolayers synthesized using chemical vapour deposition are able to retain some of the strain arising from the mismatch in thermal coefficients of expansion (TCE) between the film and the substrate, while still retaining their intrinsic optoelectronic properties [8]. This observation is intriguing, as the strain was retained for films grown on amorphous substrates. While strain stabilization arising from crystalline epitaxial growth is well documented, one might expect that remnant thermal mismatch

strain mediated by van der Waals bonding to a substrate would be relaxed during cooling from the growth temperature, as the bonding between the film and substrate is relatively weaker.

Since the strain is mediated by the bonding between the film and substrate, the strain should be relieved if the film decouples from the substrate. A method to release the TCE mismatch induced strain in WSe_2 mono- and bilayers was recently presented [9]. This solvent-evaporation mediated decoupling (SEMD) process consists in letting a droplet of acetone *evaporate* on top of a strained WSe_2 film grown on amorphous silica. The decoupling refers to the supposition that the droplet evaporation enables the film to slip upon the substrate so as to reduce its internal strain while still remaining bonded to the substrate. The strain in the 2D TMDC is released as the film-liquid-vapor triple contact line sweeps over the film. The stress in the films relaxes from the edges inward, as is shown through time-dependent photoluminescence experiments [9]. In contrast, no strain relaxation is observed when the film is completely submerged in acetone.

The effectiveness of the SEMD process raises (at least) three interesting questions. First, are the bonds formed during van der Waals epitaxy sufficiently strong to sustain the strain, or must there be some number of covalent bonds between the film and the substrate? Second, what is the nature of the perturbation to the film induced by the presence of the acetone that allows for decoupling of the film and the substrate? Third, what are the conditions under which SEMD will be operative?

2.2 Calculus of Variations

As the problem at hand requires computing the minimum energy state of a system for a given Hamiltonian, the calculus of variations is a natural choice. In this section we will be following and using notation similar to that of Ref. [11]. The objective of this section is, rather than give a comprehensive overview of the calculus of variations, to develop sufficient understanding as to arrive to Eqn. 2.19. On future sections, we will be using the calculus of variations, and specially Eqn. 2.19, to find configurations that, given a Hamiltonian, are energy extrema. We are particularly interested in configurations that minimize the energy. Let us start then with some definitions.

One can think of a functional as a "function of functions," and a general and basic functional can be written as

$$J = \int_{x_0}^{x_1} F(x, y(x), y'(x))dx, \tag{2.1}$$

where J is the functional and F is a function of the three arguments x, $y(x)$, and $y'(x)$. In this case, we see that the functional J has a definite numerical value if the function $y(x)$ is fixed, and in this sense we say that J *is a functional of* y. In "normal" calculus, our task was to find the number x in which a given function $f(x)$ had an extrema; similarly, in variational

calculus our goal is to find a function $y(x)$ in which a given functional J has an extrema. We will also say that a function f is belongs to class C_n if its derivatives up to n are continuous.

We start by considering a C_1 function $\eta(x)$ satisfying $\eta(x_0) = \eta(x_1) = 0$. If the functional J defined in Eqn. 2.1 is evaluated at $y(x)+\alpha\eta(x)$, where α is a parameter and $y(x)$ is assumed to be an extremum of the functional J, we may think of J as a function of α, that is

$$J(\alpha) = \int_{x_0}^{x_1} F(x, y(x) + \alpha\eta(x), y'(x) + \alpha\eta'(x))dx. \tag{2.2}$$

Thus, we know from calculus that $J(\alpha)$ has an extremum on $\alpha = 0$, and that $J' = 0$, that is

$$\begin{aligned} J'(0) &= \int_{x_0}^{x_1} \left[F_{,y}\eta(x) + F_{,y'}\eta(x)\right] dx \\ &= \left[F_{,y'}\eta(x)\right]_{x_0}^{x_1} + \int_{x_0}^{x_1} \eta(x) \left[F_{,y} - \frac{d}{dx}F_{,y'}\right] dx \\ &= \int_{x_0}^{x_1} \eta(x) \left[F_{,y} - \frac{d}{dx}F_{,y'}\right] dx = 0, \end{aligned} \tag{2.3}$$

where we are obviating the functional dependencies $y(x)$ and $F\left(x, y, y'\right)$, and a subscript after a comma denotes differentiation with respect to the quantity following the comma. It is easy to prove that, in order for Eqn. 2.3 to be true for an arbitrary function $\eta(x)$,

$$F_{,y} - \frac{d}{dx}F_{,y'} = 0 \tag{2.4}$$

must be satisfied. Eqn. 2.4 is called Euler's equation and is a requirement for $y(x)$ to be an extremum of J as defined in Eqn. 2.1.

We introduce notation similar to that of calculus and define the first variation of the functional J, δJ, as the product $\alpha J'(0)$. We also make the definition $\delta y \equiv \alpha\eta(x)$. With this, we can rewrite Eqn. 2.3 as

$$\delta J = \left[F_{,y'}\delta y\right]_{x_0}^{x_1} + \int_{x_0}^{x_1} \left(F_{,y} - \frac{d}{dx}F_{,y'}\right) \delta y dx \tag{2.5}$$

To obtain Eqn. 2.4 we have assumed that the value of $y(x)$ is fixed at x_0, x_1. However, this is not the case of the physical model to be presented below, were we do not restrict the displacement of the film in one of the integration limits, say the lower one. To account for this condition for the variational defined in Eqn. 2.1, we consider a function η such that $\eta(x_0) \neq 0$, and $\eta(x_1) = 0$. Then, following a derivation similar to that used to arrive to Eqn. 2.3, we get that, besides Eqn. 2.4, it is necessary for $y(x)$ to be an extrema to satisfy the boundary condition

$$F_{,y'}\Big|_{x=x_0} = 0. \tag{2.6}$$

Similarly, if the functional is of the form

$$J = \int_{x_0}^{x_1} F(x, y(x), y'(x))dx - \psi(y_0) + \phi(y_1), \tag{2.7}$$

where $y_i = y(x_i)$, the natural boundary conditions have the form

$$\psi'(y_0) + F_{,y'}\Big|_{x=x_0} = 0, \tag{2.8}$$

$$\phi'(y_1) + F_{,y'}\Big|_{x=x_1} = 0. \tag{2.9}$$

Finally, we look at the case where the integral limits are not fixed. To do this, we consider again the functional defined in Eqn. 2.1. Whereas previously we have considered a function $y(x) + \alpha\eta(x)$, it is convenient to now consider that y depends on α in a general way, i.e. $y(x) = f(x, \alpha = 0)$. We will also assume that $f(x, \alpha)$ is C_2, and that $x_i(\alpha = 0) = x_i$. With this, we have that

$$J(\alpha) = \int_{x_0(\alpha)}^{x_1(\alpha)} F(x, f(x, \alpha), f'(x, \alpha))dx. \tag{2.10}$$

To continue with our δ notation introduced earlier, we define

$$\delta x_i = \frac{dx_i(\alpha)}{d\alpha}\Big|_{\alpha=0} \alpha, \tag{2.11}$$

$$\delta y = \frac{\partial f(x, \alpha)}{\partial \alpha}\Big|_{\alpha=0} \alpha, \tag{2.12}$$

$$\delta y' = \frac{d}{dx}\delta y. \tag{2.13}$$

In this notation, the first variation of J is given by

$$\delta J = [F(x, y, y')\delta x]_{x_0}^{x_1} + \int_{x_0}^{x_1} \left(F_{,y}\delta y + F_{,y'}\delta y'\right) dx. \tag{2.14}$$

Transforming the second term in the integral by parts integration, we have

$$\int_{x_0}^{x_1} F_{,y'}\delta y' dx = F_{,y'}(x_1, y_1, y_1')(\delta y)_1 - F_{,y'}(x_0, y_0, y_0')(\delta y)_1 - \int_{x_0}^{x_1} \left(\frac{d}{dx}F_{,y'}\right) \delta y dx, \tag{2.15}$$

where

$$(\delta y)_i = \frac{df(x_i, \alpha)}{d\alpha}\Big|_{\alpha=0} \alpha. \tag{2.16}$$

It will be useful to find an expression for $(\delta y)_i$ in terms of something we know. For this, we obtain the first variation of $y_i = f(x_i(\alpha), \alpha)$:

$$\begin{aligned}\delta y_i &= \left.\frac{df(x_i(\alpha),\alpha)}{d\alpha}\right|_{\alpha=0}\alpha \\ &= \left[\frac{\partial f}{\partial x_i}\frac{dx_i}{d\alpha} + \frac{\partial f}{\partial \alpha}\right]_{\alpha=0}\alpha \\ &= y_i'\delta x_i + (\delta y)_i. \end{aligned} \tag{2.17}$$

Inserting Eqns. 2.17 and 2.15 into 2.14, we have

$$\delta J = \left[\left(F - y'F_{,y'}\right)\delta x + F_{,y'}\delta y\right]_{x_0}^{x_1} + \int_{x_0}^{x_1}\left(F_{,y} - \frac{d}{dx}F_{,y'}\right)\delta y dx. \tag{2.18}$$

Combining the arguments used to arrive to Eqns. 2.8, 2.9, and 2.14, it is possible to obtain the first variation of the functional defined in Eqn. 2.7 when the integration limits are allowed to vary:

$$\begin{aligned}\delta J = &\left[\left(F - y'F_{,y'}\right)\delta x\right]_{x_0}^{x_1} + \left[\left(F_{,y'} + \phi_{,u}\right)\delta y\right]_{x_1} - \left[\left(F_{,y'} + \psi_{,u}\right)\delta y\right]_{x_0} + \phi_{,x_1}\delta x_1 + \psi_{,x_0}\delta x_0 \\ &+ \int_{x_0}^{x_1}\left(F_{,y} - \frac{d}{dx}F_{,y'}\right)\delta y dx. \end{aligned} \tag{2.19}$$

Eqn. 2.19 is the most general function we are going to need. Thus, we can end this section and present the physical model.

2.3 Model overview

Now that we we have established the mathematical tools, we move forward to study our particular problem. For this, we will create a continuum Hamiltonian for the substrate-film-droplet-air system that takes into account the elastic, interfacial, and substrate-film interaction energies into account. As the Hamiltonian is a functional of the film's displacement, we can use the calculus of variations to find the minimum energy elastic state of the system. As this is not an easy problem, we will start from the simplest case and then scale our way to more realistic models. In Section 2.3.1 we model the case of a film strained on top of a substrate. Then, we add the droplet but preclude out-of-place displacement (OOPD) of the film. Finally, we discuss the magnitude of the OOPD. A schematic of the geometry of the model can be found in Fig. 2.1.

In order to make progress, however, there are some assumptions that are needed. The first one is that we will be considering a circular film instead of one with a triangular shape, which would be closer to the experiments [9]. The circular geometry was chosen as it leads to an axisymmetric model that can be solved relatively easily. While the geometry of the film may alter the shape of the contact patch for the droplet and the film, the underlying

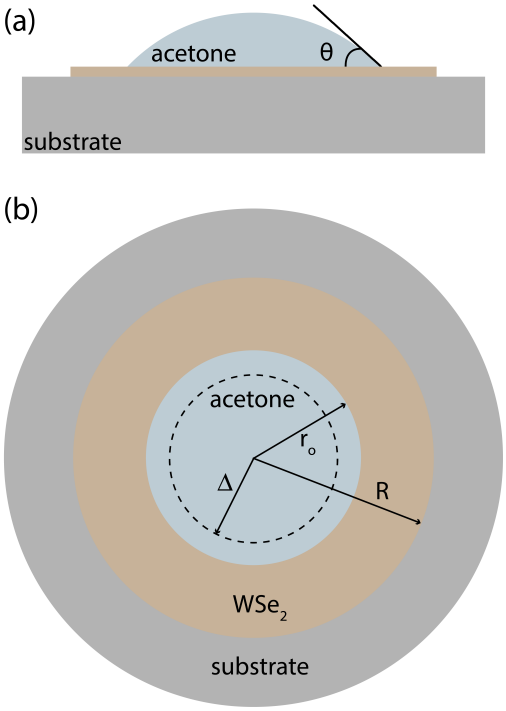

Figure 2.1: A schematic of the continuum model: (a) side view and (b) top-down view. The WSe_2 sample is assumed to be circular in shape with unstrained radius R, and rigidly attached to the substrate within the radius Δ, again defined in the unstrained material coordinate system. The material within this radius is assumed to be under the fixed biaxial strain ε_0 (that arises from the synthesis process). The radius of the contact patch between the acetone and the film is taken to be r_0, also in the unstrained material coordinate system. The contact angle θ also is shown.

physical processes will remain very similar, and the insights from the circular model will be helpful in understanding the release of the triangular samples. The change from a circular geometry to a triangular one also results in more atoms at the edge of the film, and it is reasonable to expect that these atoms might be bonded more strongly to the substrate than atoms in the interior of the film. The model does not account for differences between interior and edge atoms, but experimental results [9] prove that the force exerted by the droplet is enough to overcome any force due to extra bonds that the edge atoms might have with the substrate.

Another assumption that we make is that the film-liquid and film-vapor interfacial energies will not depend on the elastic state of the film. This is justified because the strain in the film is assumed to be small enough so that no substantial change in the nature of the bonding occurs.

2.3.1 Film over substrate

The model of a strained film on a substrate can be used to develop an understanding of the forces preventing the TCE mismatch strain from relaxing due to thermal fluctuations or other effects.

Consider the film-substrate system without the droplet. Specifically, consider the configuration in which the film is decoupled and completely free to slide beyond a radius of Δ, and is also biaxially strained by an amount ε_0 for $r < \Delta$ (see Fig. 2.1(b)). One can use continuum linear elasticity theory to estimate the magnitudes of the forces that the atoms near Δ must exert in order to keep the film stable.

The system is axially symmetric with a deformation map given by $r \to r + u(r)$, with $u(r)$ the in-plane displacement. Then, we have the restriction that

$$u\left(r\right) = \varepsilon_0 r,\ r \leq \Delta \tag{2.20}$$

Within continuum linear elasticity theory, the energy of the system is given by

$$\begin{aligned} E &= 2\pi \int_0^R E_s[r, u(r), u'(r)] r dr \\ &= 2\pi \left(\Delta^2(\lambda + \mu)\varepsilon_0^2 + \int_\Delta^R E_s[r, u(r), u'(r)] r dr \right), \end{aligned} \tag{2.21}$$

where λ and μ are the Lamé constant and shear modulus of the WSe_2 film, respectively, and

$$E_s[r, u(r), u'(r)] = \frac{(\lambda + 2\mu)\left(r^2 u'(r)^2 + u(r)^2\right) + 2\lambda r u(r) u'(r)}{2r^2} \tag{2.22}$$

is the strain energy density. As E can be thought of as the basic functional defined in Eqn. 2.1, and we do not have any restriction for $u(r)$ at $r = R$, we know that, for $u(r)$ to be an extremum, it must satisfy the Euler Eqn. 2.4 and the boundary conditions

$$\begin{aligned} u(\Delta) &= \Delta\varepsilon_0, \\ E_{s,u'} r \Big|_{r=R} &= 0. \end{aligned} \tag{2.23}$$

Solving the differential equation, one finds that the radial displacements of the film are given by:

$$u\left(r\right) = \frac{\Delta^2 \varepsilon_0 \left(\mu r^2 + R^2(\lambda + \mu)\right)}{r\left(\Delta^2 \mu + R^2(\lambda + \mu)\right)},\ r \geq \Delta, \tag{2.24}$$

and by plugging Eqn. 2.24 into 2.21, we get that the equilibrium energy of the system is

$$E_{elastic}\left(\Delta\right) = 2\pi\Delta^2(\lambda + \mu)\varepsilon_0^2 + \frac{2\pi\Delta^2\mu(\lambda + \mu)\varepsilon_0^2(R - \Delta)(\Delta + R)}{\Delta^2\mu + R^2(\lambda + \mu)}. \tag{2.25}$$

Note that, as there is only one minimum that satisfies Euler's Eqn. and the boundary conditions, and as one can easily find a displacement $u(r)$ resulting in a greater energy, we can be sure that the displacement defined in Eqn. 2.24 is the global minimum, and hence the energy in Eqn. 2.25 is the equilibrium energy for a given Δ. As Δ is the material radius up to which the film is coupled to the substrate, we can think of the force on Δ as the decoupling force, the film being totally decoupled and allowed to relax when $\Delta = 0$.

The generalized force leading to decoupling of the monolayer can be computed from the elastic energy. One finds:

$$F_\Delta = -\frac{\partial E_{elastic}}{\partial \Delta} = -\frac{4\pi\Delta R^4(\lambda+\mu)^2(\lambda+2\mu)\varepsilon_0^2}{\left(\Delta^2\mu + R^2(\lambda+\mu)\right)^2}, \tag{2.26}$$

where the negative sign indicates that the force is acting to decrease Δ, as expected. F_Δ is plotted as a function of Δ for the parameters shown in Table 2.1, a monolayer of radius $R = 8\,\mu\text{m}$, and initial strain of $\varepsilon_0 = 0.7\%$ in Fig. 2.2(a), for reference. The sample size and strain were chosen to be comparable to those studied experimentally [9], though the experimental samples are triangular. Unless otherwise noted, these parameters will be used throughout Chapter 2.

To make a quantitative estimate of the bond forces necessary to retain the strain, consider the following model. Suppose that the atoms within the $\Delta - \delta < r < \Delta$ annulus slip so as to relieve the strain within the annulus. Also assume that the atoms with positions such that $r > \Delta$ remain decoupled from the substrate, so that they can slide freely on the substrate. One can estimate the average bond force on the atoms in the considered annulus by equating the reduction in elastic energy to the work those bond forces would need to do to restrain the film to its pre-slipped configuration.

The change in elastic energy upon decoupling an annulus of thickness δ starting from a strained region of radius Δ, defined to be $\Delta E_{elastic}(\Delta, \delta)$ can be approximated by

$$\Delta E_{elastic}(\Delta, \delta) \approx F_\Delta \delta. \tag{2.27}$$

In this sense, F_Δ sets the scale for the atomic forces, and can be used to assess the changes in these atomic forces with changing parameters. However, one can make a more accurate calculation by computing the finite difference in energy directly using Eqn. (2.25), so going forward, we define $\Delta E_{elastic}(\Delta, \delta) = E_{elastic}(\Delta - \delta) - E_{elastic}(\Delta)$.

The average displacement of the atoms in the $\Delta - \delta < r < \Delta$ annulus due to the motion of the decoupling front is defined to be $\bar{u}(\Delta, \delta)$. Defining the displacement of the atoms within the annulus upon motion of the pinned region boundary by δ to be $\Delta u(r, \delta)$:

$$\Delta u(r, \delta) = \frac{\varepsilon_0(\Delta-\delta)^2\left(\mu r^2 + R^2(\lambda+\mu)\right)}{r\left(\mu(\Delta-\delta)^2 + R^2(\lambda+\mu)\right)} - \varepsilon_0 r, \tag{2.28}$$

one finds:

$$\begin{aligned} \bar{u}\left(\Delta,\delta\right) &= \frac{\int_{\Delta-\delta}^{\Delta} 2\pi r \Delta u\left(r,\delta\right) dr}{\pi\left(\Delta^2-\left(\Delta-\delta\right)^2\right)} \\ &= -\frac{2\delta R^2(2\delta-3\Delta)(\lambda+\mu)\varepsilon_0}{3(\delta-2\Delta)\left(\mu(\delta-\Delta)^2+R^2(\lambda+\mu)\right)}. \end{aligned} \tag{2.29}$$

Using this observation, the magnitude of the average force on the atoms in the region of interest, defined to be $\bar{f}\left(\Delta,\delta\right)$, is approximated by the change in elastic energy computed using Eqn. (2.25) divided by the product of the number of atoms in the strip contacting the substrate and their average displacement:

$$\begin{aligned} \bar{f}\left(\Delta,\delta\right) &= \frac{\Delta E_{elastic}\left(\Delta,\delta\right) A_c}{\bar{u}\left(\Delta,\delta\right)\pi\left(\Delta^2-\left(\Delta-\delta\right)^2\right)} \\ &= \frac{3R^2 A_c(\delta-2\Delta)(\lambda+\mu)(\lambda+2\mu)\varepsilon_0}{\delta(2\delta-3\Delta)\left(\Delta^2\mu+R^2(\lambda+\mu)\right)}, \end{aligned} \tag{2.30}$$

with A_c the area of the unit cell for the monolayer. $\bar{f}(\Delta,\delta)$ is plotted as a function of Δ for various values of δ in Fig. 2.2(b).

Care should be used in applying Eqn. (2.30). Examination of this expression shows that as $\delta \to 0$, the characteristic bond force diverges $\sim \delta^{-1}$. This implies that the average bond force must be infinite to keep the film coupled to the substrate. The difficulty, of course, is that the film is not an elastic continuum, and decreasing the radius of a coupled region by amounts less than the lattice parameter makes little sense. So applying the model for $\delta \sim$ lattice parameter is not likely to yield reasonable results. Moreover, the film may not relax smoothly on the scale of the lattice parameter, but, as discussed below, it is likely to have domains of relaxation that in turn trigger other domains to relax, etc. However, a more detailed analysis requires an atomic scale model, which is beyond the scope of this work.

Importantly, for reasonable values of δ, the model predicts that forces of the order of $0.01\,\mathrm{eV/\AA}$ are sufficient to retain the strain for reasonable values of δ. The strength of covalent bonds is of the order of $1\,\mathrm{eV/\AA}$ [12], so the bond strength necessary to sustain the strain is approximately two orders of magnitude weaker than that expected from covalent bonds. Indeed, atomic scale simulations for a strained MoS_2 monolayer system predict that, in order to maintain a tensile strain of $\sim$1%, forces with an order of magnitude of $0.01\,\mathrm{eV\,\AA^{-1}}$ per atom are needed [13]. The theory predicts that the average force per atom within a strip $50\,\mathrm{\AA}$ wide necessary to sustain the observed strain is of the order of $0.01\,\mathrm{eV\,\AA^{-1}}$. It is reasonable to expect that the slipping of the decoupling front will involve the correlated motion of atoms over a strip this wide. It is also likely that the decoupled portion of the film will, perhaps weakly, re-adhere to the substrate, further stabilizing the strain within the film. The model, which neglects this re-adhering, will overestimate the force required for stabilization. Thus it appears that a relatively thin strip of atoms weakly bonded to the surface is able to maintain the tensile strain in the film, such that it is not necessary

to invoke the presence of covalent bonds between the substrate and the film. The analysis, however, does not rule out the possibility that a small number of covalent bonds might be present.

Table 2.1: Numerical values of the material properties and the methods by which they were obtained. DFPT stands for Density Functional Perturbation Theory, and γ_{sl} was computed using Eqn. (2.31) with $\theta = 22°$. Values are in MeV Å^{-1} units.

λ [14]	μ [14]	γ_{sv}[15]	γ_{lv} [16]	γ_{sl}
144	303	0.24	0.16	0.10
DFPT		Contact angle measurement	Capillary rise	Young's equation

2.3.2 Droplet over film over substrate

After we have solved a problem using the mathematical tools developed in Sec. 2.2, and gained some understanding on the nature of the bonds maintaining the strain in the WSe_2 film, we now add the droplet to the model. The droplet is assumed to have the shape of a spherical cap and to be concentric to the film, as shown in Fig. 2.1.

2.3.2.1 No out-of-plane displacement

Empirically, it is known that the passage of the contact triple point across the surface of the film leads to decoupling and release of the stress. Evidently, the contact triple point increases the forces tending to decouple the film. In general, when considering static friction, one assumes that the frictional force is related to the normal force. One possible explanation for the decoupling of the film by the evaporating liquid droplet is that the droplet lifts the film, and reduces the friction force [9]. A detailed analysis of this possibility is presented in Sec. 2.3.2.2 where it is shown that the film is expected to lift approximately 0.01 Å, an amount that is surely negligible. Given this observation, then, the origins of the decoupling must be present in a model for which the lifting of the film is negligible. One such model is presented here.

The starting point for this model is the exploration of the deformation of a solid in the presence of a droplet. If a droplet sits on an undeformable substrate, the contact angle obeys Young's equation:

$$\gamma_{lv}\cos(\theta) + \gamma_{sl} - \gamma_{sv} = 0, \tag{2.31}$$

where θ is the contact angle between the substrate and the liquid; the subscripts l, v, s stand for liquid, vapor and solid, respectively; and γ_{ij} is the specific interfacial free energy of the ij interface. It is well known, however, that if the substrate is deformable, Eqn. (2.31) is no longer valid [17–25]. While there are several models describing this system [23, 26–28], the film under consideration is bound to a substrate that resists the vertical deflection, as noted above.

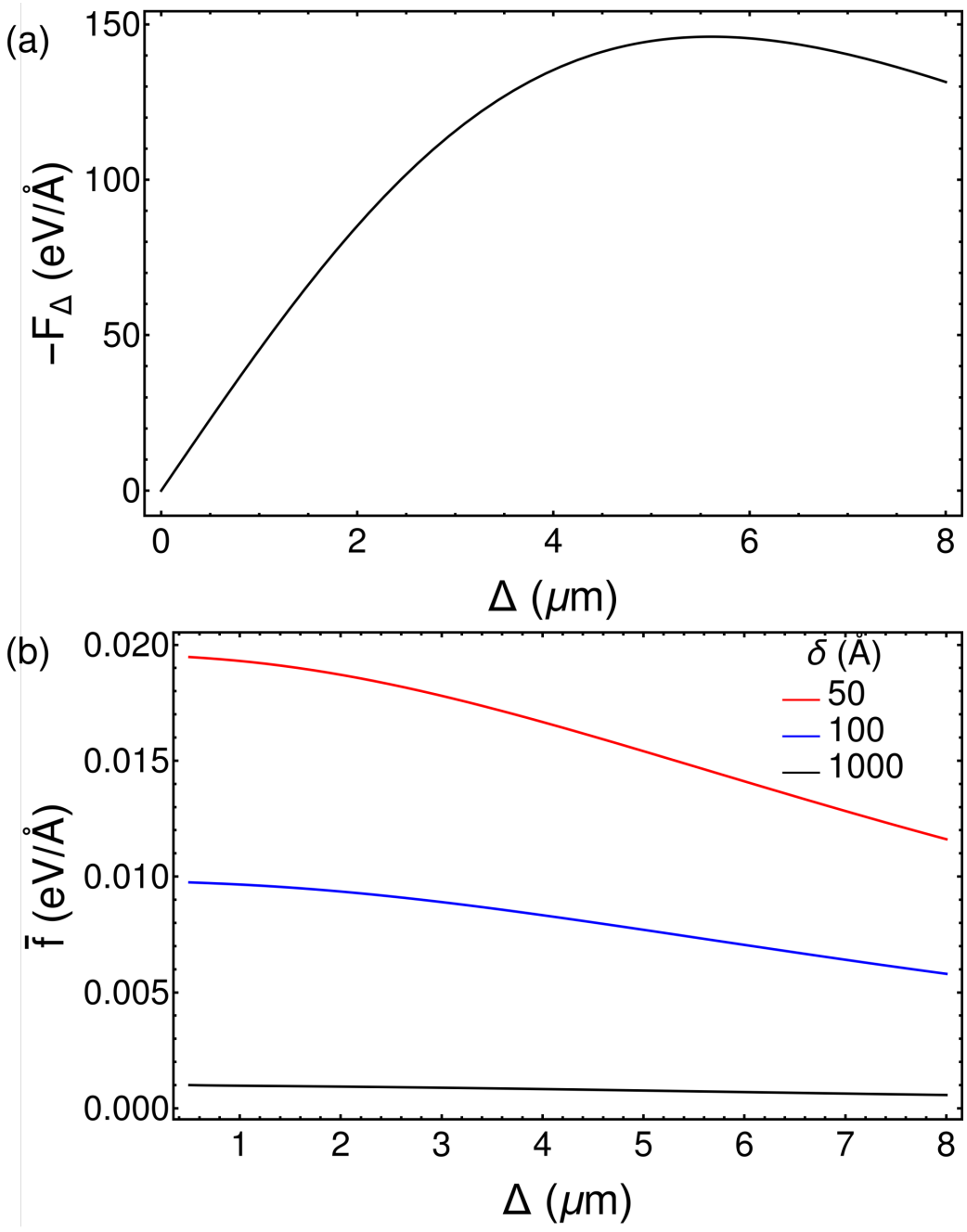

Figure 2.2: (a) The generalized force on the decoupling boundary plotted as a function of Δ. (b) An estimate of the average force per atom experienced by atoms with $\Delta - \delta \leq r \leq \Delta$ computed as described in the text plotted vs. Δ for three different values of δ. The magnitudes of these forces are approximately two orders of magnitude below the range associated with covalent bonding.

Therefore, we suppose that a spherical cap droplet is supported by a material that is only allowed to have in-plane deformation. Physically, this corresponds to a thin film supported on a rigid substrate, with the interaction between the film and substrate strong enough to prevent out-of-plane deformations. Considering the droplet to be centered on the film, the problem remains axisymmetric, and the deformation map can also be written as $r \to r+u(r)$. The distance from the center of the droplet to the triple contact line is defined to be $r_0 + u_0$, with $u_0 = u(r_0)$. As in Sec. 2.3.1, it is assumed that $u(r) = \varepsilon_0 r$ if $r \leq \Delta$.

First, consider the case in which the film is submerged in liquid, i.e. $r_0 > R$. In this instance, the elastic energy of the film changes as Δ is decreased from $\Delta = R$, but the interfacial energies remain constant (in the approximation that any film strain dependence to the liquid/film interfacial free energy can be neglected); then, the system reduces to that presented in Sec. 2.3.1. Similarly, if $r_0 \leq \Delta$, the deformation of the film will not have any effect on the interfacial energy of the system, as the film-liquid-vapour triple contact line sits is on the undeformable region; in this case, the forces in the system are also reduced to those computed in Sec. 2.3.1. Thus for the droplet to influence the decoupling process, the edge of the droplet must fall in the film's deformable region, *i.e.* $\Delta < r_0 < R$, and this will be assumed in what follows.

With the droplet present, the total energy of the system is given by

$$\begin{aligned} E = {} & 2\pi \left(\varepsilon_0 \Delta\right)^2 (\lambda + \mu) + \pi \Delta^2 \gamma_{sl} + \\ & + 2\pi \left(\int_{\Delta}^{r_0} \left(\gamma_{sl} + E_s[r, u(r), u'(r)]\right) r dr + \int_{r_0}^{R} \left(\gamma_{sv} + E_s[r, u(r), u'(r)]\right) r dr \right) + \\ & + \gamma_{lv} A_{lv}, \end{aligned} \tag{2.32}$$

where the first two terms on the right hand side correspond to the elastic and interfacial energy in the $0 \leq r < \Delta$ region, respectively; A_{lv} is the liquid-vapor interface area; and E_s is the strain energy density, defined in Eqn. 2.22. In order for the energy E in Eqn. 2.32 to have the form of a sum of previously studied functionals (Eqn. 2.7), an expression for A_{lv} in terms of the boundary values of u_0 and r_0 is needed. To do this, we start by considering the volume of a spherical cap with base radius $d = r_0(1+\varepsilon)$ and contact angle θ, which is given by

$$V = \frac{\sqrt{A_{lv}} \left(A_{lv} + 2\pi d^2\right) \sqrt{1 - \frac{\pi d^2}{A_{lv}}}}{6\sqrt{\pi}}. \tag{2.33}$$

Solving for A_{lv}, linearizing in the strain ε, and then doing the replacement $\varepsilon r_0 \to u_0$, one finds:

$$
\begin{aligned}
A_{lv}(r_0,u_0,V) =& \frac{2\pi^{7/3}r_0^5u_0\left(\sqrt{\pi^2r_0^6+9V^2}+3V\right)}{\sqrt{\pi^2r_0^6+9V^2}\left(6V\left(\sqrt{\pi^2r_0^6+9V^2}+3V\right)+\pi^2r_0^6\right)^{2/3}}+\\
&+\frac{\pi^{5/3}r_0^3\left(2u_0\left(\sqrt{\pi^2r_0^6+9V^2}+3V\right)+r_0\sqrt{\pi^2r_0^6+9V^2}\right)}{\sqrt{\pi^2r_0^6+9V^2}\left(6V\left(\sqrt{\pi^2r_0^6+9V^2}+3V\right)+\pi^2r_0^6\right)^{1/3}}+\\
&+\left(6\pi V\left(\sqrt{\pi^2r_0^6+9V^2}+3V\right)+\pi^3r_0^6\right)^{1/3}-\pi r_0(r_0+2u_0). \qquad (2.34)
\end{aligned}
$$

The in-plane displacement function can be defined as a piecewise function

$$
u(r)=\begin{cases} r\varepsilon_0 & r<\Delta \\ u_1(r) & \Delta\le r\le r_0 \\ u_2(r) & r_0\le r\le R, \end{cases} \qquad (2.35)
$$

subject to boundary conditions

$$
\begin{aligned}
&u_1(r_0)=u_2(r_0)=u_0 \text{ and}\\
&u_1(\Delta)=\varepsilon_0\Delta. \qquad (2.36)
\end{aligned}
$$

To work our way to the first variation of the energy, it is useful to group the full energy of the system, Eqn. (2.32), as follows:

$$
E=\underbrace{\int_\Delta^{r_0}F_1[u_1(r),u_1'(r),r]\,dr}_{E_1}+\underbrace{\int_{r_0}^{R}F_2[u_2(r),u_2'(r),r]\,dr}_{E_2}+\phi(r_0,u_0), \qquad (2.37)
$$

where

$$
F_i=2\pi r\left(\gamma_{si}+E_s[u_i(r),u_i'(r)]\right), \qquad (2.38)
$$

$\gamma_{s1}=\gamma_{sl}$, $\gamma_{s2}=\gamma_{sv}$, and

$$
\phi(r_0,u_0)=2\pi\left(\varepsilon_0\Delta\right)^2(\lambda+\mu)+\pi\Delta^2\gamma_{sl}+\gamma_{lv}A_{lv}(r_0,u_0). \qquad (2.39)
$$

Then, the variational of the energy can be written as

$$
\delta E=\delta E_1[u_1,u_1';r_0]+\delta E_2[u_2,u_2';r_0]+\delta\phi(r_0,u_0), \qquad (2.40)
$$

where E_1 and E_2 are functionals of the in-plane displacement u, u', and also depend on r_0; on the other hand, ϕ is a function of the parameters r_0 and u_0. As there are no physical constraints for the values of $u_1(r_0)$, $u_2(r_0)$, and $u_2(R)$ (that is, other than the continuity

constraint $u_1(r_0) = u_2(r_0)$) natural boundary conditions are used. Thus, the variationals of the individual terms in Eqn. (2.40) are given by

$$\begin{aligned}
\delta E_1 = &\int_\Delta^{r_0} \left(F_{1,u_1} - \frac{d}{dr} F_{1,u_1'} \right) \delta u_1 dr + \\
&+ \left(F_1 - u_1' F_{1,u_1'} \right) \Big|_{r=r_0} \delta r_0 + \\
&+ F_{1,u_1'} \Big|_{r=r_0} \delta u_1(r_0), \qquad (2.41) \\
\delta E_2 = &\int_\Delta^{r_0} \left(F_{2,u_2} - \frac{d}{dr} F_{2,u_2'} \delta u_2 dr \right) + \\
&+ F_{2,u_2'} \Big|_{r=R} \delta u_2(R) + \\
&- \left(F_2 - u_2' F_{2,u_2'} \right) \Big|_{r=r_0} \delta r_0 + \\
&- F_{2,u_2'} \Big|_{r=r_0} \delta u_2(r_0), \qquad (2.42) \\
\delta \phi = &\phi_{,r_0} \delta r_0 + \phi_{,u_0} \delta u_0, \qquad (2.43)
\end{aligned}$$

where the functional dependencies have been obviated. Then, grouping terms, we have that

$$\begin{aligned}
\delta E = &\\
&\int_\Delta^{r_0} \left(F_{1,u_1} - \frac{d}{dr} F_{1,u_1'} \right) \delta u_1 dr \qquad (2.44a) \\
&+ \int_{r_0}^{R} \left(F_{2,u_2} - \frac{d}{dr} F_{2,u_2'} \right) \delta u_2 dr \qquad (2.44b) \\
&+ \left(F_1 - u_1' F_{1,u_1'} - F_2 + u_2' F_{2,u_2'} + \gamma_{lv} A_{lv,r_0} \right) \Big|_{r=r_0} \delta r_0 \qquad (2.44c) \\
&+ \left(F_{1,u_1'} - F_{2,u_2'} + \gamma_{lv} A_{lv,u_0} \right) \Big|_{r=r_0} \delta u_0 \qquad (2.44d) \\
&+ \left(F_{2,u_2'} \right) \Big|_{r=R} \delta u_2(R). \qquad (2.44e)
\end{aligned}$$

Since all the variations are arbitrary, one can assume that each of the terms (2.44a) - (2.44e) vanish independently.

Consider terms (2.44a) and (2.44b). Since δu_i is an arbitrary variation, one concludes that $F_{i,u} - \frac{d}{dr} F_{i,u'} = 0$. Using the definition of F_i, Eqn. (2.38), and solving the resulting second order differential equation, one finds

$$u_i(r) = a_{i1} r + \frac{a_{i2}}{r}, \qquad (2.45)$$

where a_{ij} are constants to be determined. Using the boundary conditions (2.36), and setting term (2.44e) equal to zero, it is possible to write three of the undetermined constants a_{ij} in terms of a_{11}:

$$\begin{aligned} a_{12} &= \Delta^2(\varepsilon - a_{11}), \\ a_{21} &= \mu\frac{a_{11}\left(r_0^2 - \Delta^2\right) + \Delta^2\varepsilon}{r_0^2\mu + R^2(\lambda+\mu)}, \\ a_{22} &= R^2(\lambda+\mu)\frac{a_{11}\left(r_0^2 - \Delta^2\right) + \Delta^2\varepsilon}{r_0^2\mu + R^2(\lambda+\mu)}. \end{aligned} \tag{2.46}$$

An analytical expression for a_{11} as a function of r_0 can be derived from setting term (2.44d) to zero. Lastly, it is possible to compute a numerical value for r_0 by setting term (2.44c) to zero. Then, with this solution, the equilibrium configuration of the system and its energy are determined from Eqns. (2.32), (2.45), and (2.46), along with the expression for a_{11} and the numerical value of r_0.

2.3.2.2 Out-of-plane displacement

Allowing for the film to have out-of-plane displacements (OOPDs) will change the model in three main ways. First, some of the liquid will be wrapped by the film, resulting in a decrease of A_{lv}; if this is to happen spontaneously, this will necessarily decrease the liquid-vapour interfacial energy. Second, the substrate-film interaction has to be taken into account. Finally, the elastic energy of the film, previously given by (2.22), needs to be modified to account for the OOPD. We can estimate the extent of the OOPDs by looking at how the energy of the system changes when these additional terms are considered.

The deformation map of the film is given by $\{r,\, 0\} \rightarrow \{r + u(r),\, f(r)\}$, where $f(r)$ is the OOPD at radius r. If the film is lifted at r_0, a portion V_w of the liquid volume V will be wrapped by the film. Assuming that the length of the OOPD feature of the film near r_0 is small compared to R, and that far from r_0 the film is at the equilibrium height (set at $f(r) = 0$), we have

$$V_w = 2\pi\int_0^{r_0}\left(r + u(r)\right)\left(1 + u'(r)\right)\left(f_0 - f(r)\right)dr \approx \pi f_0\left(r_0 + u_0\right)^2, \tag{2.47}$$

where $f_0 = f\left(r_0\right)$. Then, the liquid-vapour interfacial energy is given by

$$E_{lv} = \gamma_{lv}A_{lv}\left(r_0, u_0, V - V_w\right). \tag{2.48}$$

The substrate-film interaction energy is fit to a Morse potential:

$$E_{subs-film} = 2\pi\int_0^R rD_e\left\{1 - \exp\left[-\beta\left(r - r_{eq}\right)\right]\right\}^2 dr, \tag{2.49}$$

where D_e, β are constants. To determine D_e and β, Density Functional Theory (DFT) computations were run using the Vienna Ab initio Simulation Package [29–31] version 5.4.4.

The projected-augmented-wave method was used to model the core electrons [32], and the exchange-correlation energy was estimated using Perdew-Burke-Ernzehof functionals [33]. All the simulations were run using a 500 eV cutoff energy for the plane-wave basis set, a Γ-centered k-point $8 \times 8 \times 1$ grid, and convergence criteria of 10^{-4} eV for the electronic self-consistent cycle. The simulations consisted in a 27 layer slab of α-SiO_2 with a reconstructed (001) surface, as reported in Ref. [34]; a 3×3 monolayer WSe_2 supercell was positioned on top of the SiO_2; to obtain a commensurate structure, the SiO_2 was put under a -0.3% biaxial compression. The parameters in Eqn. (2.49) were obtained by fitting the energies obtained by DFT, the results being $D_e = 0.50\,\text{meV}\,\text{Å}^{-2}$ and $\beta = 1.31\,\text{Å}^{-1}$. The energies, along with a the Morse fit, are shown in Fig. 2.3.

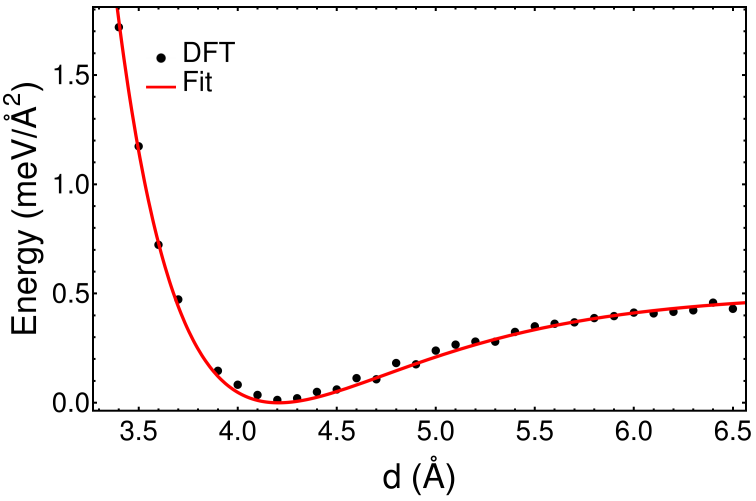

Figure 2.3: Energy of WSe_2/SiO_2 system as a function of the film-substrate separation, d. The solid line is Eqn. (2.49) using $D_e = 0.50\,\text{meV}\,\text{Å}^{-2}$ and $\beta = 1.31\,\text{Å}^{-1}$

The elastic energy will now have to account for the bending energy. Using linear elasticity theory, we find:

$$E_{bending} = \pi\kappa \int_0^R r \left(\frac{f'(r)}{r} + f''(r) \right)^2 dr, \tag{2.50}$$

where $\kappa = 11.25\,\text{eV}$ [35] is the bending rigidity. Also, the strain energy density is modified to incorporate OOPD:

$$E_s = \frac{1}{8}(\lambda + 2\mu)\left(f'(r)^2 + 2u'(r)\right)^2 + \frac{\lambda u(r)\left(f'(r)^2 + 2u'(r)\right)}{2r} + \frac{(\lambda + 2\mu)u(r)^2}{2r^2}. \tag{2.51}$$

Using a Gaussian-like function for the OOPD,

$$f(r) = f_0 \exp\left[-\frac{(r - r_0)^2}{\sigma} \right], \tag{2.52}$$

and Eqns. (2.48-2.51), the energy of the system was evaluated, and the differences in energy of these systems compared to the case were no OOPD is allowed, ΔE_{OOP}, are plotted in Fig. 2.4. Note that, as we are not solving the variational equations for this case, the form of the displacements used to obtain the energies shown in Fig. 2.4 are not the ones that minimize the energy; this is justified because the goal of this section is not to determine a precise value for f_0, but rather to assess its orders of magnitude. The values reported in the figure were obtained by choosing the value of σ to minimize the energy change for each value of f_0; for the reported f_0 range, it was found that the values of σ that minimized the energy were in the $240\,\text{Å}^2 < \sigma < 250\,\text{Å}^2$ range, corresponding to an OOPD feature of $\sim 50\,$Å. Fig. 2.4 shows a reduction of the energy of about 2 eV related to the lifting of the film. While this energy is big on an atomic scale, it is minuscule compared to the liquid-vapor interfacial energy, which is in the order of tens of MeV. Also, note that the f_0 range in which an energy reduction happens is very narrow, with the minimum occurring around $f_0 = 0.0125\,$Å. This level of OOPDs will not alter much the analysis as compared to assuming no OOPD, and is consequently neglected.

2.4 Results and discussion

The hypothesis investigated here assumes that the strained film will be near instability, and that the strain release will be governed by a type of near-critical behavior found in other systems governed by stick/slip friction. Theoretical analysis of pinned charge density waves [36], earthquake fault slipping [37] and dislocation motion [38–40] all show that in such systems, a small perturbation force can lead to a large scale response. In the present case, we propose that a small perturbative force can initiate the slipping process that relaxes the film.

In this framework, then, all that is needed is for the droplet to provide the necessary perturbing force. The theory presented here shows that there is an in-plane force arising from the liquid/vapor/solid intersection.

If the droplet is considered, the elastic state of the film is a function of the interfacial energies γ_{ij}, meaning that it will be different from that shown in Sec. 2.3.1. To understand the extra force provided by this perturbation, we begin by comparing the in-plane displacements u of the equilibrium configuration in systems with and without a droplet, Fig. 2.5. For the chosen interfacial tensions [which correspond to $\theta < \pi/2$ in Eqn. (2.31)], the displacements within the decoupled region are reduced relative to the values that they have in the absence of the droplet. *The implication is that the droplet places the region $\Delta < r < r_0$ under compression relative to the droplet-free case.* This additional compressive strain exerts a force on the boundary of the decoupled region tending to decrease Δ. Hence, for the chosen parameters, the presence of a droplet with $\Delta < r_0 < R$ increases the decoupling force.

Note that the increase in decoupling force is of the order of a few percent (see Fig. 2.6) – an amount consistent with the notion that the films are near instability. That the extra force increases with the droplet volume may explain why sometimes, as reported in Ref. [9],

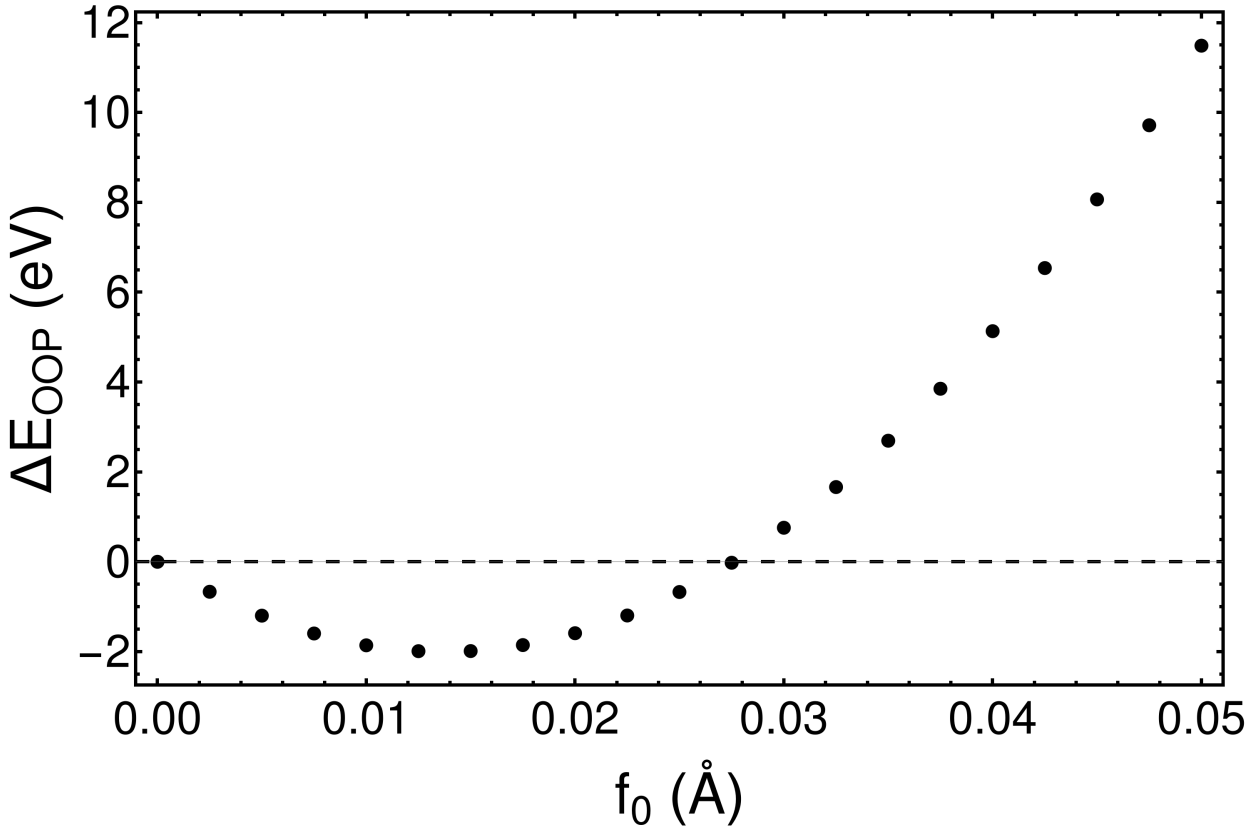

Figure 2.4: Energy differences of systems with and without OOPD. The parameters used where those shown in Table 2.1, $V = 150\,\mu m^3$, $\Delta = 5\,\mu m$. The values for r_0 and u_0 were obtained using the formalism shown in Sec. 2.3.2.1

it takes several droplet applications in order to fully relax the film. As the the volume of the droplet decreases due to evaporation, the extra force may fall below the threshold necessary to trigger decoupling causing the radius of the contact patch of the droplet to fall below Δ. Reapplying another, larger drop, increases the force, and enables decoupling to proceed.

Also note that in the presence of the strain, the contact angle defined by Eqn. (2.31) is not the final contact angle of the fluid. Since the film is strained, and the strain exerts a force on the triple point, the contact angle is altered slightly. The angle might be decreased or increased depending upon the sign of the stress, and the value of the contact angle for an unstressed film.

In order to assess the conditions in which the SEMD is possible, one has to consider how the system will behave for a variety of parameter sets and strains. Though the mathematics underlying the effect of an evaporating droplet are subtle, there is a simple way to qualitatively predict the effects of droplet evaporation on the decoupling. If the in-plane projection of the liquid-vapor interfacial tension anti-aligns with the radial displacements arising from

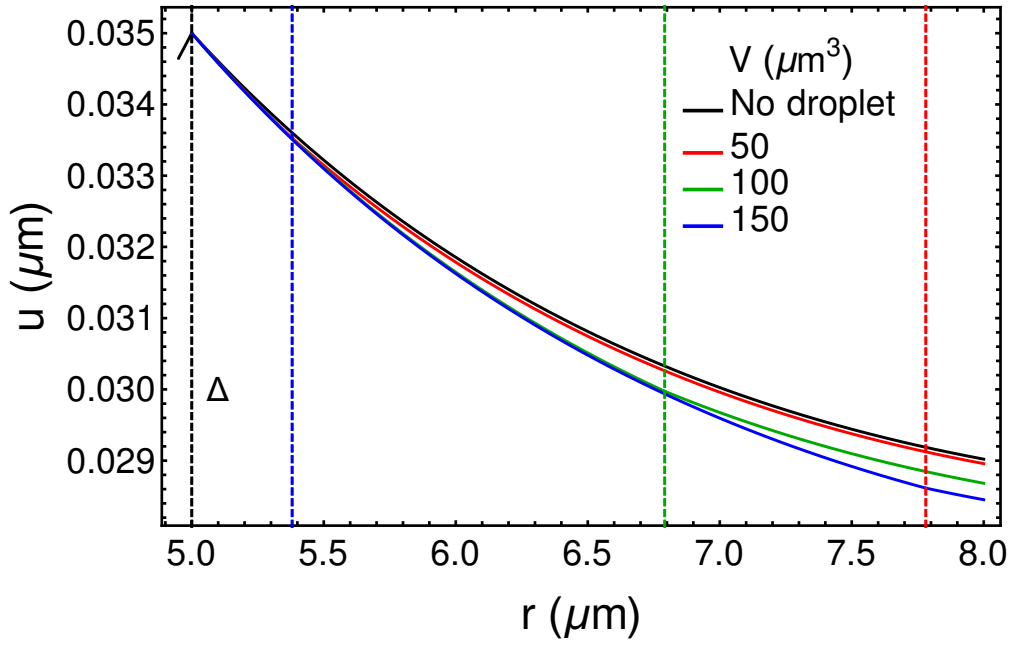

Figure 2.5: In-plane displacement in the equilibrium configuration for a system with $\Delta = 5\,\mu\text{m}$ and different liquid volumes. The vertical black line corresponds to $r = \Delta$, while the others correspond to $r = r_0$ for the different values of V

the initial strain (radially outwards if $\varepsilon_o > 0$, radially inwards if $\varepsilon_o < 0$), the evaporation will increase the net force on the decoupling interface, and can lead to decoupling. Conversely, if the projection of the liquid-vapor interfacial tension is aligned with the displacements associated with ε_0, the evaporating droplet will tend to stabilize the strain state. The applicability of this simple assessment is presented in Fig. 2.7. This figure shows, for a variety of contact angles as defined by Eqn. (2.31), the displacements, $u_d(r)$ and the strains $\varepsilon_d(r) = u_d'(r)$, induced by the application of an evaporating droplet. Note that the displacements plotted here are computed according to

$$u_d(r) = u^{\text{with droplet}}(r) - u^{\text{without droplet}}(r) \tag{2.53}$$

with $u^{\text{with droplet}}(r)$ and $u^{\text{without droplet}}(r)$ referring to the solutions for the displacements with and without the droplet, respectively. From the ε_d plots shown in the third column of Fig. 2.7, one can see the effect the droplet has on the decoupling force F_Δ: if ε_d is of the opposite sign of ε_o in the $\Delta < r < r_0$ region, as in cases I and IV, then the decrease in the elastic energy prompted by a decrease in Δ is bigger than in the no droplet case, thus increasing $|F_\Delta|$, and the droplet has the potential to initiate strain release. In contrast, in cases II and III, the strain release will not be initiated.

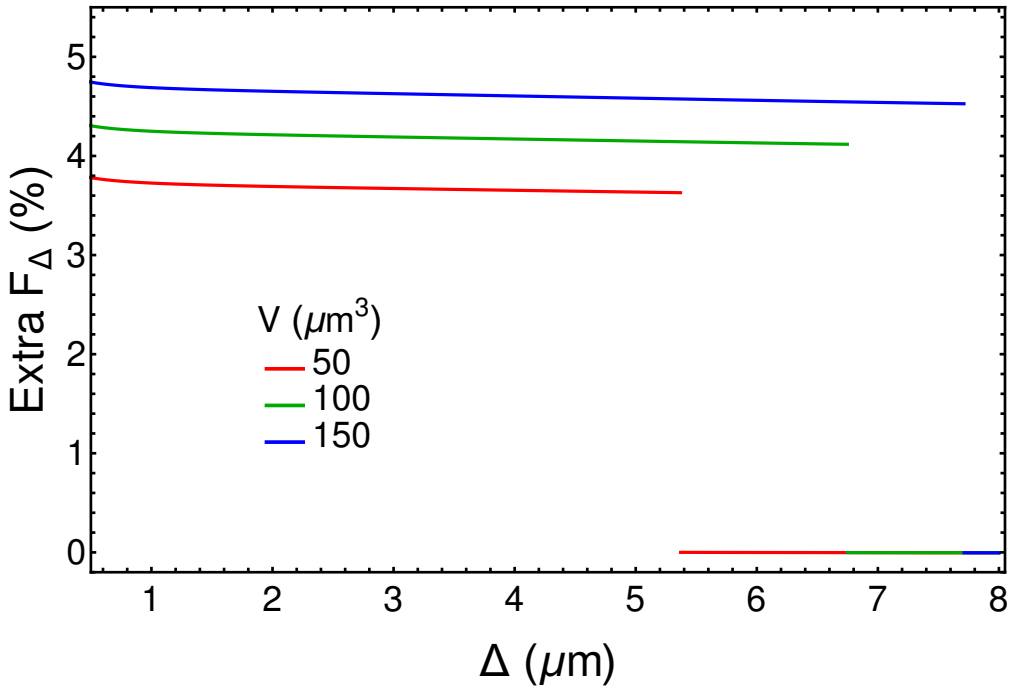

Figure 2.6: Percentage increase in decoupling force (now elastic plus droplet effects) relative to just the elastic force for three different droplet volumes plotted as a function of Δ. The step discontinuity at larger Δ arises from the fact that, within the model, there is no extra force if the radius of the pinned region is larger than the radius of the droplet contact patch.

2.5 Conclusion

This chapter presents a theoretical model for the SEMD method for as-grown strain release in a film is developed and analyzed. The model demonstrates that bond strengths well below those of covalent bonds are likely sufficient to stabilize the strains arising during the van der Waals epitaxial growth of the WSe_2. The model also predicts that a droplet of liquid can generate an additional in-plane force that can trigger the decoupling of the film from the substrate. Specifically, if the contact angle of the liquid is such that the projection of the liquid/vapor surface tension is anti-aligned with the elastic displacements of the coupled film, then the in-plane force has the potential to trigger decoupling.

The origin of the extra decoupling force is the compression (or tension, depending upon the system in question) of the outer portion of the film that is free to slide. This additional strain arises from the interfacial tensions associated with the droplet/film/vapor triple point. For the acetone/WSe_2 strained in tension samples, the extra compression of the free sliding region from the droplet can be relieved if more of the film decouples by reducing Δ, and the droplet can initiate strain release. The extra decoupling force represents an approximate 4% increase in the decoupling force for the specific case of an acetone droplet and a WSe_2 film

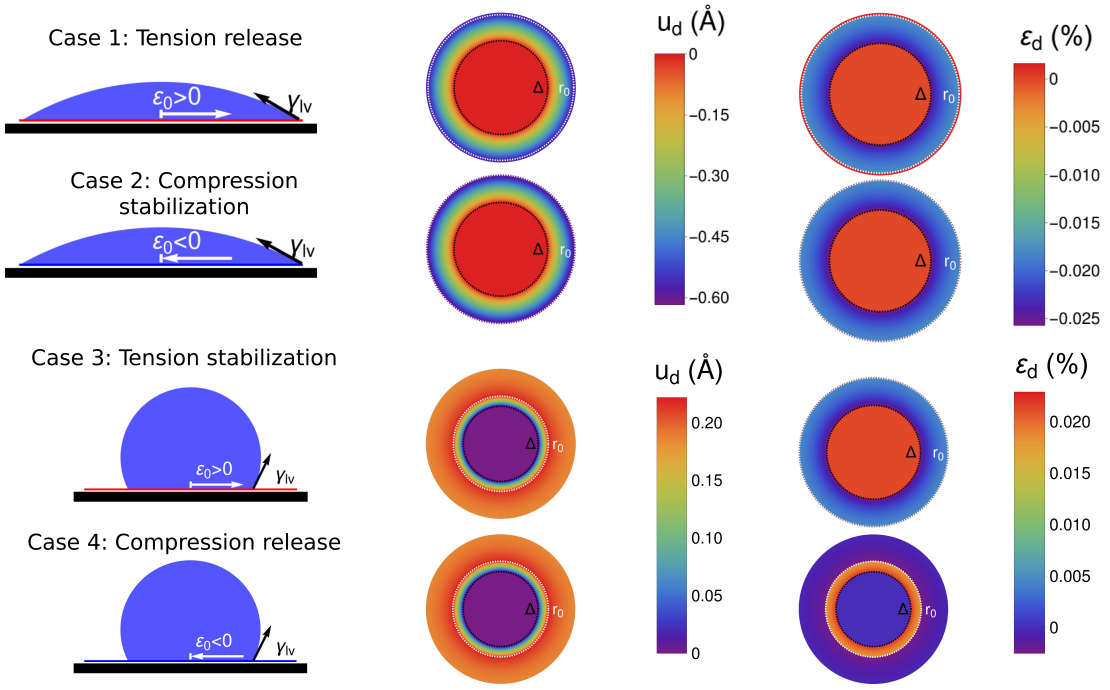

Figure 2.7: Schematics, displacement and strains for a droplet on top of a strained film. For cases 3 and 4, a volume of $V = 500\,\mu m^3$ was used; $\gamma_{lv} = 0.45\,\mathrm{MeV}^2\,\mu m^{-1}$ and $\gamma_{sl} = 0.40\,\mathrm{MeV}^2\,\mu m^{-1}$ were selected so that γ_{lv} would match that of water and the Young's angle, defined by Eqn. (2.31), was 110°. Cases 2 and 4 use an initial strain of $\varepsilon_o = -0.7\%$. The white arrows indicate the direction of the displacements associated with the strain. For cases 1 and 4, the droplet has the potential to initiate decoupling of the film from the substrate. For cases 2 and 3, the droplet will likely stabilize the strain state.

grown on amorphous silica.

Based on the model, it may be possible to use the SEMD method with a wide range of substrates and 2D materials beyond TMDCs, opening the possibility of creating complex relaxation patterns that exploit the strain tuned direct-to-indirect bandgap change [4] to create novel devices. The fundamental understanding of the origins of the extra force provided by the droplet, and the predictions outlined in Fig. 5, make the case for the SEMD method to be a viable pathway to engineer strain in 2D materials, thereby harnessing the variety of strain-tunable properties [41].

Chapter 3

Tellurium crystalline thin film growth

After being studied in the 1980s due to their applications in data storage materials [42–45], tellurium thin films are nowadays experiencing a revival due to its potential application in semiconductor devices [46–49] and their appealing optical and electronic properties [50–52]. On top of this, their crystal structure, depicted in Fig. 3.1, is composed of triangular chains arranged in an hexagonal fashion. While it has been established that the bonds within the chains are covalent, the nature of the interchain bonds is still being debated [53]. When growing films on unheated substrates from vapor, most materials tend to form amorphous slabs because of the lack of kinetic energy needed for the atoms to rearrange themselves in the lower-energy crystalline state; thus, a high-temperature annealing step may be needed for crystallization. Interestingly, Te grown by physical vapor deposition (PVD) crystallizes at near-ambient temperature, and films grown this way are found to have respectable electrical properties when the experimental conditions are optimized [50, 54–56].

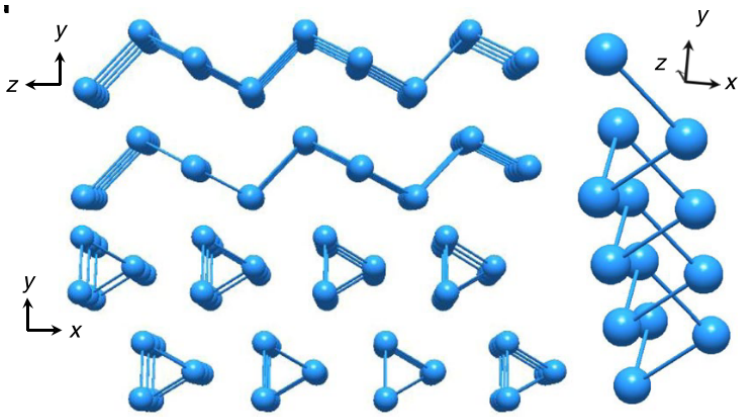

Figure 3.1: Crystal structure of Te.

Even though research has been done in the direction of finding optimal conditions for Te thin film growth, the amorphous to crystalline phase transition kinetics are yet to be fully

understood. This chapter aims to provide a theoretical framework for the amorphous to crystalline phase transition. In section 3.1, we detail the experiments from which data for our model was extracted. Section 3.2 gives a brief introduction to both the Johnson-Mehl-Avrami-Kolmogorov (JMAK) mathematical model for nucleation and growth and classical nucleation theory (CNT), and section 3.3 introduces the image analysis methods used to quantify the experimental data. Finally, results are presented in section 3.4 while conclusions are drawn in section 3.5. This chapter is based in the work presented in Ref. [50].

3.1 Experimental details

In a chamber starting at 2×10^{-6}mbar, Te atoms were deposited by thermal evaporation in a SiO_2/Si substrate kept at $-80\,^{\circ}$C by a cold nitrogen gas flow. When the deposition process ended, the sample was taken out of the chamber after it reached $5\,^{\circ}$C to prevent water condensation from ambient air. Immediately after unloading them from the chamber, samples were put in a thermoelectric module that was previously set at a desired temperature.

As the crystallization process did not start before loading the sample in the thermoelectric module, this experimental set up allowed the recording of the crystallization process at different temperatures using optical microscopy. Moreover, Te anisotropic optical properties made it possible to differentiate between crystals with different orientations using polarized light. From the videos of the crystallization process, it is possible to obtain kinetic parameters such as the growth rate, while grain number density can be extracted from the polarized light micrographs.

3.2 Nucleation and growth phenomena

Before analyzing the experimental data, we must first set the data that we want to extract. The following sections are a concise introduction to a mathematical model of nucleation and growth, and of the physical causes behind these phenomena.

3.2.1 Johnson-Mehl-Avrami-Kolmogorov model

The JMAK model [57–60] considers the phase transformation of a material in which nuclei of the new phase are appearing at a rate $\dot{N}$ (units of number of new nuclei per area per time), and these nuclei have a linear growth rate v (units of length per time). In what follows, we will consider constant growth and nucleation rates, isotopic growth, and a 2D material.

We start by considering the growth of a single crystalline nucleus created at time τ. The area of this seed after t time has passed if given by

$$a_1(t) = \pi v^2 (t-\tau)^2. \tag{3.1}$$

Considering the growth at an infinitesimal period of time, we get

$$da_1(t) = 2\pi v^2 (t-\tau) dt. \tag{3.2}$$

If we are to consider several nuclei appearing and growing in the same material, care should be taken, as impingement, i.e. nuclei growing into one another, must be accounted for. Labelling the total area of the material as A and the untrasformed area as $A_u(t)$, the fraction of untransformed area is given then by $u(t) = A_u(t)/A$. If nucleation is totally random, then $u(t)$ is, in average, the fraction of the nuclei that lies on an untransformed area. Thus, the mean area contributed to the transformation by a single nuclei in an infinitesimal time dt is given by

$$da_2(t) = u(t)da_1(t) = 2\pi v^2 u(t)(t-\tau)dt. \tag{3.3}$$

Considering a completely untransformed material, the number of new nuclei formed in an infinitesimal interval $d\tau$ is

$$dN_0 = A\dot{N}d\tau. \tag{3.4}$$

Note that, even though Eqn. 3.4 applies only at the very beginning of the transformation, it is possible to account for the appearance of new nuclei in already transformed areas by considering random nucleation and using the fraction $u(t)$. Hence, the transformed area in an interval dt due to all nuclei nucleated at the interval $d\tau$ is

$$dN_0 da_2(t) = 2\pi A\dot{N}v^2 u(t)(t-\tau)dtd\tau. \tag{3.5}$$

From Eqn. 3.5, we find that the growth rate of the transformed area due to every nuclei, $A_c(t)$, is

$$\frac{A_c(t)}{dt} = 2\pi A\dot{N}v^2 u(t)\int_0^t (t-\tau)d\tau = \pi A\dot{N}v^2 t^2 u(t). \tag{3.6}$$

As $A_c(t) = A - A_u(t)$, we get, using the definition of $u(t)$:

$$f(t) \equiv \frac{A_c(t)}{A} = 1 - u(t), \tag{3.7}$$

where we have defined the transformed fraction as $f(t)$. From Eqn. 3.7, we have that

$$\frac{A_c(t)}{dt} = -A\frac{du(t)}{dt}. \tag{3.8}$$

Inserting Eqn. 3.8 into 3.6, and solving the differential equation with the boundary condition $u(t=0) = 1$, we have

$$f(t) = 1 - u(t) = 1 - \exp\left(-\frac{\pi}{3}\dot{N}v^2 t^3\right). \tag{3.9}$$

Furthermore, we can compute the total number of nuclei after the crystallization process has finished. To do this, we consider the number of nuclei appearing on an interval $d\tau$:

$$dN = A\dot{N}u(t)d\tau, \tag{3.10}$$

where we have assumed again that the nuclei are appearing in random positions. We then get the final grain number density, ρ, by integrating from $\tau = 0$ to $\tau = \infty$:

$$\rho = \frac{1}{A}\int_0^\infty dNd\tau = \left(\frac{3}{\pi}\right)^{1/3}\left(\frac{\dot{N}}{v}\right)^{2/3}\Gamma\left(\frac{4}{3}\right) \approx 0.879\left(\frac{\dot{N}}{v}\right)^{2/3}, \tag{3.11}$$

where Γ is the Euler gamma function.

3.2.2 Classical nucleation theory

Section 3.2.1 presented a mathematical model for nuclei of a new phase appearing and growing. Here, we will deal with the physics of why is this new phase appearing on the first place, and relate nucleation and growth rates to fundamental thermodynamic quantities like the free energy difference. The following is a presentation of some useful results from classical nucleation theory (CNT).

Consider the crystalline nuclei in an amorphous matrix. Within the CNT framework, it is assumed that this nuclei will change size by the attachment or detachment of atoms, and that there is no correlation in successive attachment or detachment events. Labelling the attachment rate to an i-cluster as $\Gamma^+(i)$, it is possible to prove [61] that the nucleation rate is given by

$$\dot{N} = n(1)\left(\sum_{i=1}^{i_{max}-1}\frac{n_{eq}(1)}{n_{eq}(i)}\frac{1}{\Gamma^+(i)}\right)^{-1}, \tag{3.12}$$

where $n(i)$ and $n_{eq}(i)$ are the number of crystalline nuclei with i atoms in the steady and equilibrium stage of the crystallization process, respectively, and i_{max} is such that $n(i_{max}) = 0$.

Using thermodynamics consideration, we can obtain the fraction of transformed nuclei with i atoms in the equilibrium state as

$$\frac{n_{eq}(i)}{n_{eq}(1)} = \exp\left(-\frac{\Delta G(i)}{k_B T}\right), \tag{3.13}$$

where k_B is the Boltzmann constant and $\Delta G(i) = -g_{c\to a}i + \gamma i^{2/3}$, with $g_{c\to a}$ the difference in free energy per atom of the amorphous and crystalline phase and γ a factor associated to the interfacial energy of the crystal in the amorphous matrix. Plugging Eqn. 3.13 into 3.12, approximating the sum by an integral and integrating around the critical number of atoms i_c for which $\Delta G(i)$ is maximum, we thus obtain

$$\dot{N} = n(1)\Gamma^+(i_c)\sqrt{\frac{\eta}{2\pi k_B T}}\exp\left(-\frac{\Delta G(i_c)}{k_B T}\right), \tag{3.14}$$

where $\eta = \frac{9g_{c\to a}^4}{8\gamma^3}$. Finally, as the attachment rate is also a thermally activated process, it can be modelled by an Arrhenius like equation. Thus, from Eqn. 3.14, we get

$$\dot{N} \approx \dot{N}_0 \exp\left(-\frac{\Delta E_v + \Delta G(i_c)}{k_B T}\right), \tag{3.15}$$

where ΔE_v is an energy barrier associated with the attachment of an atom from the amorphous matrix to the crystalline nuclei.

Lastly, approximating the nuclei as spherical, we arrive at the expression

$$\Delta G(i_c) = \frac{16\pi\gamma^3}{3\Delta G^2_{c\to a}}, \tag{3.16}$$

with $\Delta G^2_{c\to a}$ the free energy difference per volume between the crystalline and amorphous phases.

3.3 Image analysis

In this section we will describe the image analysis algorithms used to extract the data from the optical light videos and the polarized light micrographs. From the optical light videos, time series of the crystallized fraction were obtained from samples held at different temperatures. Grain number densities were extracted from polarized light micrographs.

We start by describing the three algorithms used to extract the information about the transformed fraction from the crystallization videos at different temperatures. In the simplest one, we transformed the video frames to gray scale images and selected two reference frames, one before the transformation has started and another after the system has completely crystallized. The values of the individual pixels of these reference frames are added up and labelled l_0 and l_1, for the amorphous and crystalline references, respectively. Then, the transformed fraction of the frame corresponding to time t is given by

$$f_1(t) = \frac{l(t) - l_0}{l_1 - l_0}, \tag{3.17}$$

where $l(t)$ is the sum of the value of the individual pixels of the frame corresponding to time t.

A more sophisticated version of the aforementioned algorithm was also used. In this scheme, the transformed fraction for a pixel i at time t, $p_i(t)$, was computed using the equation

$$q_i(t) = \frac{p_i(t) - p_{i,0}}{p_{i,1} - p_{i,0}}, \tag{3.18}$$

where $p_{i,0}$ and $p_{i,1}$ are the values of pixel p_i in the amorphous and crystalline reference frames, respectively. Then, the total transformed fraction for the frame is given by

$$f_2(t) = \sum_i q_i(t). \tag{3.19}$$

In the third and last algorithm that we used, we also worked with the frames extracted from the videos. The frames were then processed as follows: first, they were rescaled to 150×113 pixels. A highpass filter with a cutoff frequency of 0.025 was then applied, and the

obtained images were then transformed to gray scale. A background image corresponding to the amorphous state was selected. We define the $N(t)$ matrices as

$$N(t) = \mathrm{R}[M(t) - M_0], \tag{3.20}$$

where $M(t)$ and M_0 are the matrix representations of the processed frames corresponding to time t and to the reference state, and $\mathrm{R}[M]$ is just a rescaling function that ensures that all the values of the matrix M are between 0 and 1. The entries of the $N(t)$ matrices where then binarized by a function of the form

$$b_h(N_{ij}(t)) = \begin{cases} 1 & \text{if } N_{ij} \geq h, \\ 0 & \text{if } N_{ij} < h. \end{cases} \tag{3.21}$$

Finally, the transformed fraction was obtained by

$$f_3(t) = \frac{\sum_{ij} b_h(N_{ij}(t))}{N}, \tag{3.22}$$

where N is the total number of pixels. It is important to note that this method depends on the threshold h defined in Eqn. 3.21.

The three methods were applied to the video of the sample held at 10 °C. We can see that, even though the same reference images were used, the transformed fraction obtained using the third method, f_3, differs somewhat significantly from f_1 and f_2, with the difference increasing as the threshold h decreases.

As the first method is the simplest of the three, and it does not have any adjustable parameter besides the selection of the reference frames, results obtained using this method are the ones reported. A comparison of the results obtained using different methods can be found in Table 3.1, where we can see that, even though the shapes of transformed fraction curves obtained by using different methods differ for a given temperature (see Figure 3.2), properties of the system that are obtained by fitting the data of the curves over a range of temperatures yield similar results.

Method	ΔE_g (eV)	ΔE_N (eV)
1	0.92 ± 0.08	1.1 ± 0.2
2	0.92 ± 0.08	1.1 ± 0.2
3, h=0.44	0.82 ± 0.07	1.1 ± 0.2

Table 3.1: Values of different system properties obtained using different methods to extract data from the videos. The process to calculate these properties is explained in Sec. 3.4

To obtain the grain density of samples held at different temperatures, images obtained by polarized optical microscopy (see Figure 3.3.(a)) were analyzed. To count the number of grains, we used the Fiji software [62] to process the images as follows: first, contrast was

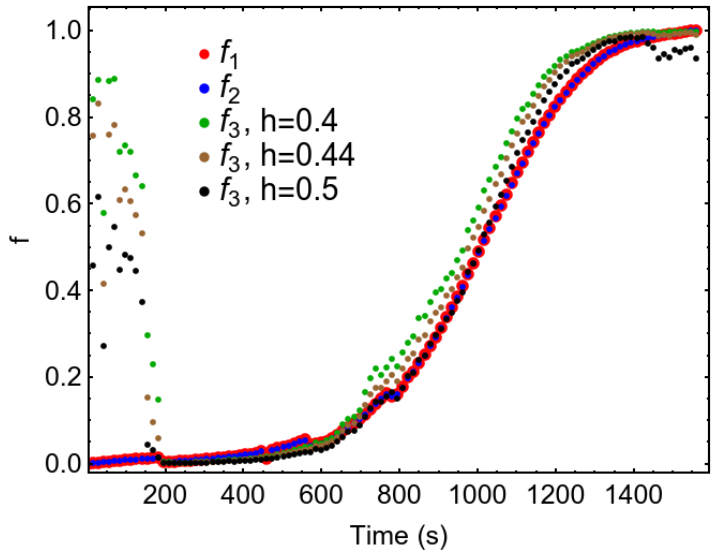

Figure 3.2: Transformed fraction for the sample held at 10 °C computed used the three methods with the same reference images.

enhanced using histogram stretching and allowing 0.3% of the pixels to saturate; then, the images were transformed from RGB to Luminance; finally, the statistical region merging algorithm [1] with 25 independent random variables per pixel was applied. The output of this process can be found in Figure 3.3. From the number of grains, it is straightforward to obtain the nuclei density; these results are shown in Figure 3.4.

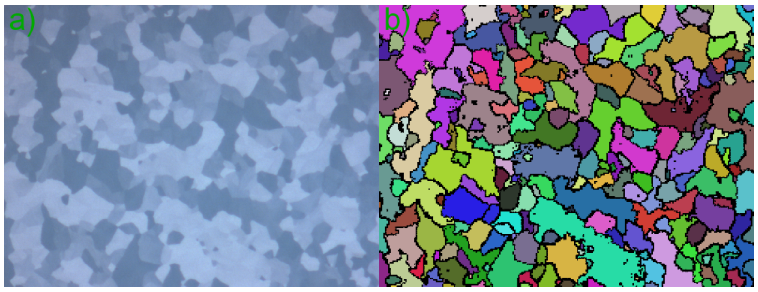

Figure 3.3: a) Polarized optical microscopy of a sample after the crystallization was completed holding the sample at 15 °C. b) Processed version of (a). The image segmentation was done using the statistical region merging algorithm [1] using 25 random variable per pixel. Region colors were assigned just to facilitate differentiation.

To extract the grain growth velocity from the videos, these were processed and analyzed using Wolfram Mathematica [63]. The processing and analysis for each video frame was done as follows: First, all the images were converted to gray scale. Then, a background image

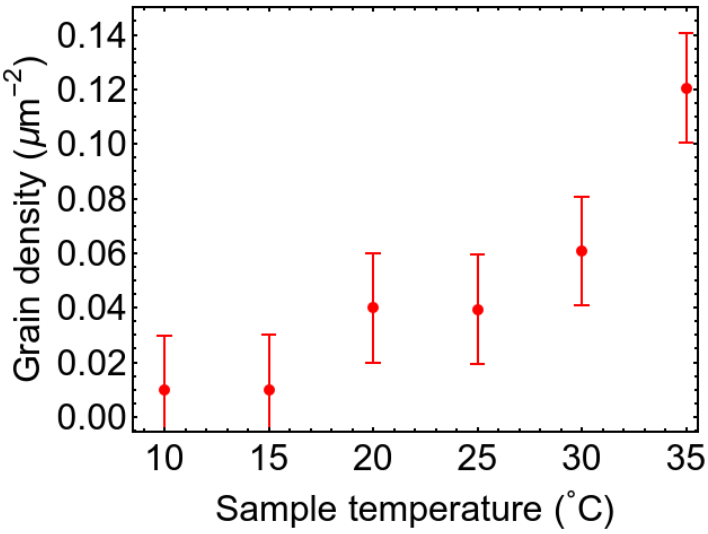

Figure 3.4: Grain density obtained by segmenting the micrographs of Te samples crystallized at different temperatures. Error bars were set to $0.02\,\mu m^{-2}$ to account for errors in the digitization of the data.

was created by averaging all the images corresponding to times previous to crystallization. Second, as the crystals are clearly brighter than the amorphous sections, all the images were binarized by comparing to the background image. Finally, the growth rates were obtained by fitting an ellipse to crystals before coalescence using the *ComponentMeasurements* package and tracking its major and minor axis growth. An example of the ellipse fit and the results obtained using this method can be found in Figure 3.5.

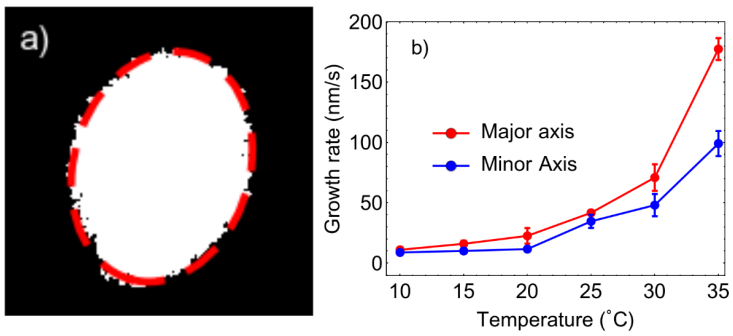

Figure 3.5: a) Binarized image of a grain and its fitted ellipse. b) Growth rate of the major and minor axis of the fitted ellipses for different temperatures. Error bars were obtained as the standard deviation of at least 3 tracked crystals.

3.4 Results and discussion

Fitting the transformed fraction data extracted from the optical light videos to Eqn. 3.9, we get an experimental measurement of the product $v^2\dot{N}$. Figure 3.6 shows the fitted curves obtained by using Mathematica's [63] *NonlinearModelFit* function as compared with the experimental data. Equation (3.9) represents the experimental data well.

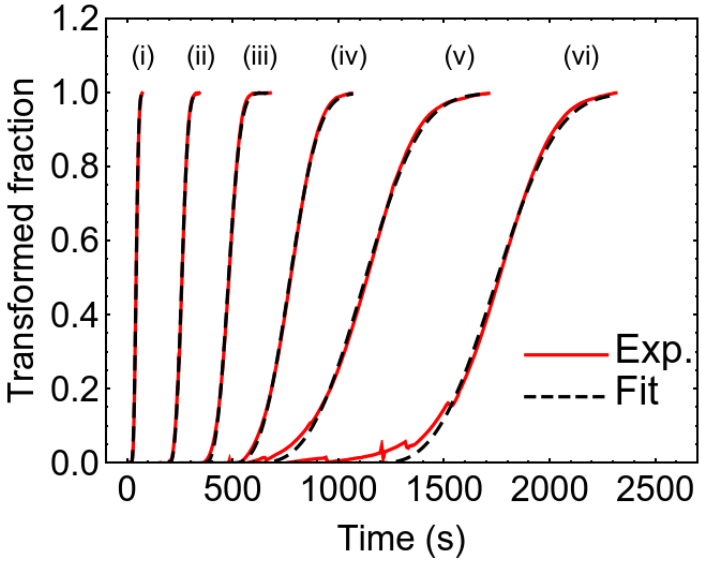

Figure 3.6: The kinetic growth data obtained from analysis of experimental data for (i)...(vii) = 35, 30, 25, 20, 15, and 10°C, respectively. The solid red curves are the experimental data obtained from the digitized movies, and the black dashed curves represent the fits of the data to Eqn. 3.9.

Now, using the grain number density values extracted from the polarized light and Eqn. 3.11, we can obtain an experimentally measured value of $\dot{N}/v$. Hence, it is possible to obtain values for $\dot{N}$ and v for each temperature at which the sample was held. Such values can be found in Fig. 3.7.

The computed radial growth rates range from 0.014 μm sec^{-1} to 0.100 μm sec^{-1}. Assuming that the growth facet is (111), this corresponds to completion of an additional atomic layer approximately every 10^{-3} sec. Assuming an Arrhenius form, the growth rate corresponds to an energy barrier of $\Delta E_v = 0.92 \pm 0.08$eV. This, presumably, is the average energy barrier for attachment of an atom to the growing cluster from the amorphous surroundings.

The nucleation rate also obeys an Arrhenius form, but with a total energy barrier of 1.99 ± 0.16eV. Using Equation 3.15 and the experimentally determined activation energies, we conclude that $\Delta G(i_c) = 1.08 \pm 0.24$eV. The Materials Project tabulates the air/crystal surface energies for Te and these range from 5 meV Å^{-2} to 23 meV Å^{-2} [64]. Assuming that the interfacial energy for the crystalline/amorphous interface is approximately half of this

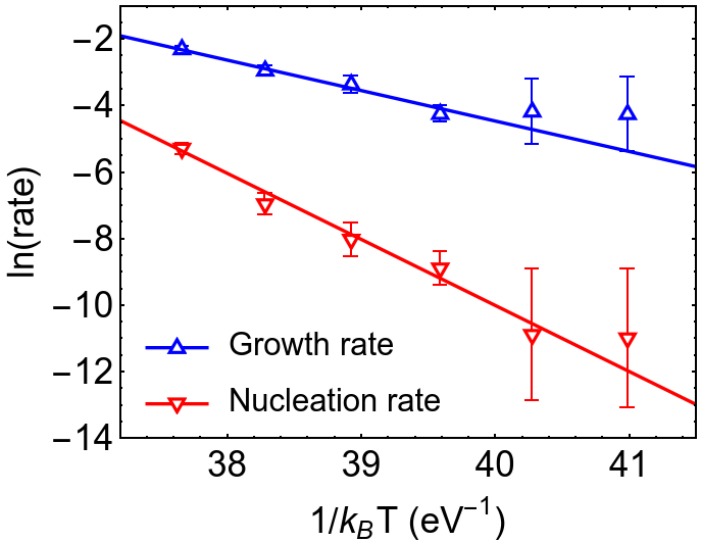

Figure 3.7: Growth and nucleation rates determined by the fitting of Eqn. (3.9) and final grain number densities. All lengths are measured in microns, and times in seconds.

energy, i.e. $\gamma = 2.5\,\text{meV}\,\text{Å}^{-2}$, using Eqn. 3.16 one concludes that $\Delta G_{c-a} = 17 \pm 7\text{meV}$ per atom, and the critical nucleus size over the temperature range studied includes approximately 127 atoms.

As temperature is decreased from 35 °C to 10 °C, the incubation time, that is, the time it takes to have a 5% transformation increases from 30 seconds to more than 10 minutes due to the suppressed nucleation rate ($\dot{N}$ is dominated by temperature) and crystallization time increases from seconds to hours (Fig. 3.8), which is contributed by low nucleation and growth rates.

The activation energy for Te crystal growth is extracted directly by measuring growth rate at different crystallization temperatures and fitting the temperature-dependent growth rate to the Arrhenius equation for grain growth (Fig, 3.9). The extracted activation energy extracted directly from measurements of growth is $0.81 \pm 0.1\text{eV}$ in good agreement with the value $\Delta E_v = 0.91 \pm 0.11\text{eV}$ extracted from fitting to Eqn. 3.9. The energy barrier is also much lower than that of Si or Ge ($\sim 3\,\text{eV}$)[65], which explains the tendency toward crystallization of the amorphous Te films at the low temperature (−10 °C or lower).

3.5 Conclusions

Based on the observations above, larger grain size can be obtained by reducing the ratio $\dot{N}/v$, which according to Eqn. 3.15 has an Arrhenius form. Consequently, over the range of temperatures modeled here, a lower temperature corresponds to a lower number of grains.

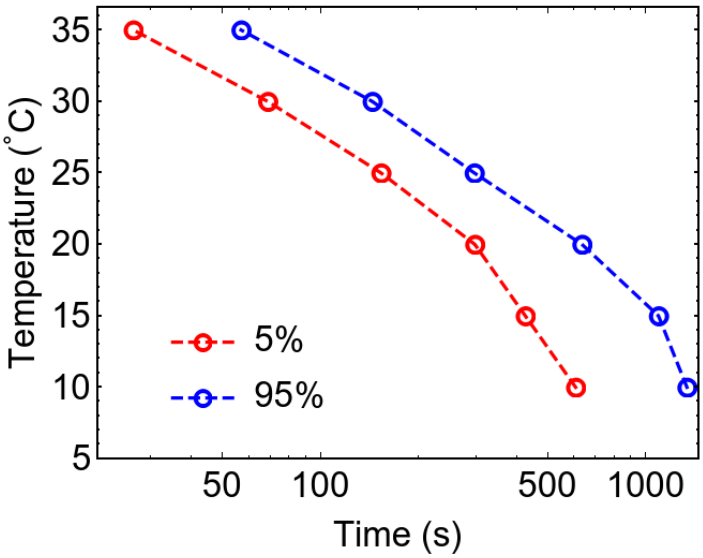

Figure 3.8: Temperature time transformation diagram for Te films crystallized at different temperatures. 5% and 95% means the coverage of the crystallized Te extracted from Fig. 3.6

Lower temperature, however, also causes the sample to crystallize at a much slower rate, and thus this process might not be readily scalable.

As the the experimental data can be fitted with good accuracy to equations obtained from the JMAK and CNT models, we know that the assumptions of each of these models also apply to the physical system at hand. The knowledge gained by the applications of these theories was used to control the crystallization process of thermally evaporated amorphous Te.

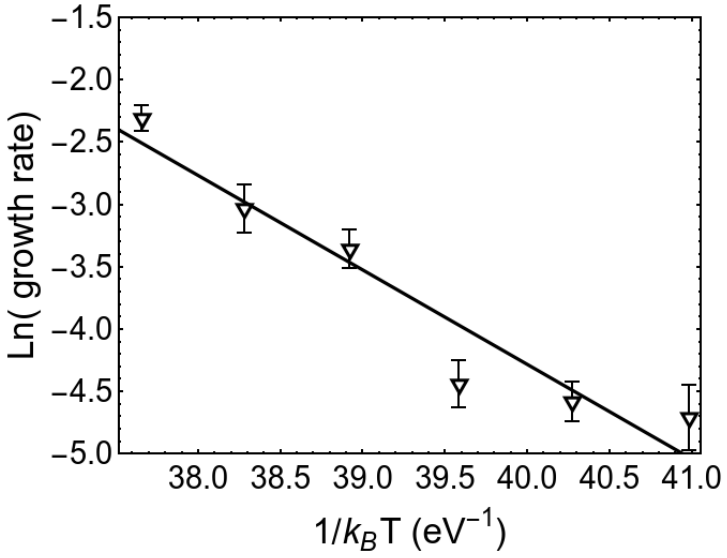

Figure 3.9: Plot of growth rate as function of temperature, measured in $\mu m\, s^{-1}$. The solid line represents the fit to an Arrhenius equation.

Chapter 4

Oriented growth of thin Te crystals

In Sec. 3 we studied the possibility of synthesizing large areas of single-crystal Te by tuning the growth parameters. While we concluded that the nucleation rate can be lowered by decreasing the temperature of the substrate, we also established that under these conditions the growth rate of the nuclei is very slow, making the process hard to scale. Then, a new, scalable method of creating high-quality, large areas of Te thin films is needed, and we present such process here.

In this chapter, instead of aiming at growing single-crystal Te thin films by suppressing the nucleation rate, we present a method for multiple Te crystals aligned in the same direction. To do this, we take advantage of the low symmetry of the Te crystalline structure (see Fig. 3.1), and use similar substrates to favor a specific chain direction. Te was grown using physical vapor deposition (PVD) on top WSe_2, WS_2, $MoSe_2$, MoS_2, and WTe_2 substrates. Of the substrates used,WSe_2, WS_2, $MoSe_2$, MoS_2 have a three-fold rotation axis, while WTe_2 has a two-fold one.

The synthesized Te films were shown to have their *c*-axis oriented in-plane, meaning that the chains were perpendicular to the vector normal to the substrate. Also, because of the high anisotropy of their bonding, Te crystals showed a needle-like growth, leading to poor area coverage. Then, different growth temperatures, as well as pre-annealing the substrate (i.e., annealing before Te depostion) were systematically explored. This section presents results previously published in Ref. [66].

4.1 Results and discussion

When Te was grown on top of substrates with a three-fold rotation axis, optical and scanning electron microscopy (SEM) images confirmed that the chains were aligned along one of the three substrate's high-symmetry directions, as can be seen in Fig. 4.1, showing a Te film on a WSe_2 pre-annealed substrate at 300 °C that was grown at 100 °C. It was also confirmed by transmission electron microscopy that the chains preferred to be aligned along armchair directions.

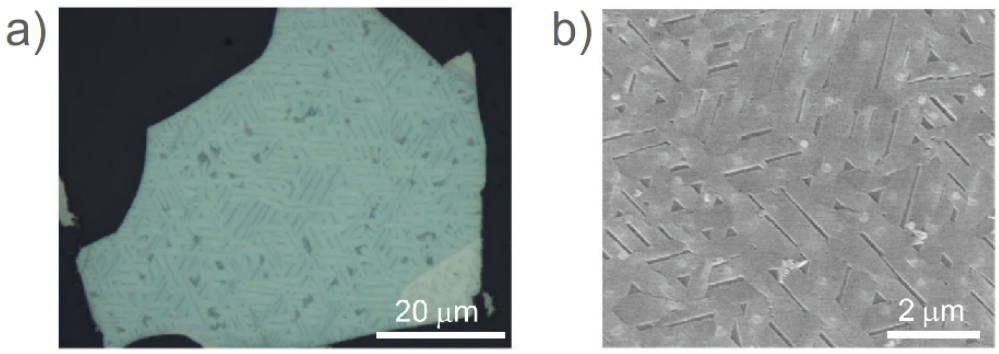

Figure 4.1: Optical (a) and SEM (b) images of the oriented ultrathin Te on WSe_2 substrate.

Substrates were also subjected to thermal treatment before the deposition process, and it was found pre-annealing increased the Te thin film coverage, as shown in Fig. 4.2. In Fig. 4.2a), Te showed a 1D needle-like structure on the untreated, as-exfoliated WSe_2 flakes. 79% of the flakes exhibited preferred growth orientation along the armchair directions, while the other 21% flakes grew along the zigzag directions. Te grown on the annealed substrates tends to form 2D structures as shown in Fig. 4.2b), c). The yield of armchair oriented flakes increases to 93% after a pre-annealing of WSe_2 substrate at 200 °C. The flakes, retaining the oriented nature, grow and merge into a film with a surface coverage of 95% on the WSe_2 substrate pre-annealed at 300 °C. Fig. 4.2a)–c) indicate that the films are more uniform after pre-annealing. We further investigate the influence of substrate temperature on the growth. Te was grown on the annealed WSe_2 flakes (annealing temperature was 300 °C) at temperatures ranging from 100 to 170 °C. As shown in the Fig. 4.2d)–f), the morphology of Te changes from 1D needle-like structure to 2D form with the growth temperature decreasing at fixed substrate preparation conditions.

The observed patterns of growth can be rationalized within a simple model. Fig. 4.3 highlights the kinetic processes that appear to be relevant to the growth mechanism. Te atoms are deposited on the surface, diffuse on that surface, and can desorb from the surface (Fig. 4.3a)–c)). Note that diffusion of adatoms on a substrate with 3-fold symmetry is expected to be isotropic. The diffusing atoms can encounter trapping sites before desorption. In the case that the trapping site is another diffusing atom, a nuclei may begin to form, growing through the attachment of additional diffusing atoms (Fig. 4.3e)). Alternatively, the trapping site might be a surface defect, such as a Se vacancy in the substrate, or a Te substitutional defect in the substrate (Fig. 4.3f)). Finally, an adatom can encounter a stable cluster of Te atoms, and begin to diffuse along its edge (Fig. 4.3d)). At the first stages of nuclei growth, i.e., when the film is thin enough for the Te-substrate van der Waals interaction to be important throughout the whole nuclei, van der Waals epitaxy takes place and Te chains align with the substrate. At later stages of growth, atoms can attach directly to existing Te islands, and thus thicken the films (Fig. 4.3g)). At this later stage, the only van der Waals interaction at play is the one between the Te chains; the difference in bond

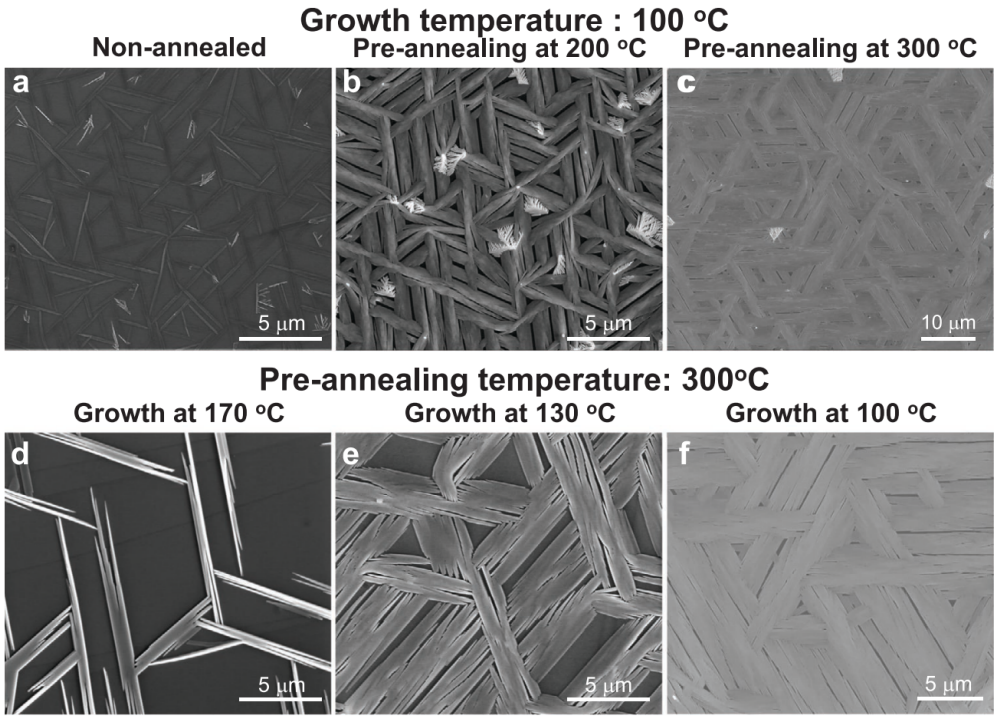

Figure 4.2: Morphology of Te grown on WSe_2 under different conditions. a–c) Te grown at 100 °C on the non-annealed (a), 200 °C (b) and 300 °C (c) annealed WSe_2 substrates. d–f) Te grown at temperatures of 170 °C (d), 130 °C (e) and 100 °C (f) on the 300 °C pre-annealed WSe_2 substrates.

strength (covalent between atoms in the same chain, van der Waals between chains) might be the mechanism behind surface roughening.

These processes can be used to understand the morphology of the growth. First and foremost, the growth shape of the crystals is determined by the relative rates of diffusion along the wire, versus diffusion at its ends. Since the Te interchain bonds are primarily of van der Waals character, one expects that edge diffusion (4.3d)) will be very rapid relative to the diffusion of Te atoms on a pristine (0001) surface because those Te are covalently bonded to the chains. These relative rates explain the aspect ratio of the growing wires, as well as the fact that the (0001) facets of the growing plates are very rough, and perhaps even display a fingering instability [67].

To further explore this matter, DFT calculation were run using the Vienna Ab Initio Simulation Package [29–31] version 5.4.4. The projected-augmented-wave method was used to model the core electrons, and the exchange-correlation energy was estimated using Perdew-Burke-Ernzehof [33]. All the simulations were run using a 600 eV cutoff energy for the plane-wave basis set, a minimum spacing for the k-points of 0.25 $Å^{-1}$, and convergence criteria of 10^{-5}eV for the electronic self-consistent cycle. Also, a dipole correction was

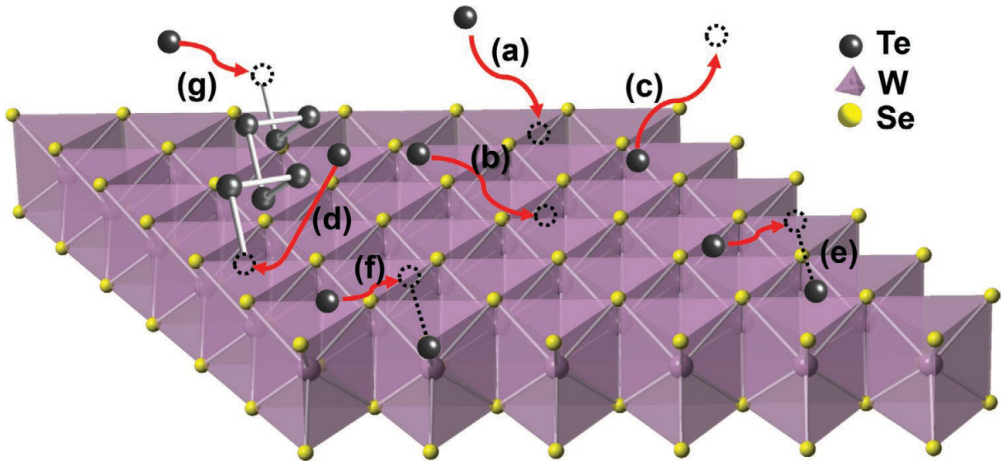

Figure 4.3: Kinetic Processes Affecting Morphology. a) Atoms arrive at the surface from the vapor. b) Atoms diffuse on the surface and c) may desorb from the surface, if they do not encounter a trapping site. d) Existing nuclei can serve as a trapping site. Once an atom encounters a wire, it is loosely bound and diffuses along the edge of the wire rapidly until it encounters the end of the wire, where it covalently bonds to the chain. e) Other atoms may also serve as trapping sites, leading, through standard nucleation kinetics, to homogeneous nucleation. f) Pre-existing defects can also serve as trapping sites, and can lead to heterogeneous nucleation. (Here the defect is a substitutional impurity atom.) g) After growth has progressed for some time, atoms will attach directly to nucleated clusters, and multilayer growth can ensue.

used in the direction perpendicular to the substrate to reduce spurious interaction of the system with its periodic image. To compute the binding energies of Te atoms to WSe_2 substrates with and without Se vacancies, a 5×5 substrate supercell was used, and the atomic positions and volume of the supercell were relaxed until the forces on all atoms were less than 10^{-3}eV Å^{-1}. Lastly, the binding energies were computed using the usual equation, $E_b = E_{Te/WSe_2} - (E_{WSe_2} + E_{Te})$, where E_{Te} is the energy of a single Te atom (obtained using a single k-point and the above mentioned parameters), and E_{Te/WSe_2}, E_{WSe_2} are the energies of Te plus substrate and substrate Te systems respectively. The binding energy of a Te slab with its substrate was computed using a supercell containing 1×4 and 1×3 substrate and Te unit cells, respectively, and strains of $\varepsilon_{33} = -3.6\%$ and $\varepsilon_{11} = -2.0\%$ were imposed on the Te slab. The bonding energy was obtained using the equation

$$E_b = \frac{E_{Te/WSe_2} - (E_{WSe_2} + E_{Te})}{A} \tag{4.1}$$

where E_{Te/WSe_2}, E_{WSe_2}, E_{Te} are the energies of the systems consisting of just the substrate, the Te slab, and the substrate plus the slab; and A is the area perpendicular to the substrate normal.

The potential for desorption helps to explain the fact that the growth rate of the films depends upon temperature and pre-annealing conditions. First, DFT total energy calculations suggest that the binding energy of the Te film to the substrate is quite weak, $10\,\mathrm{mJ\,m^{-2}}$, which is consistent with a high probability for desorption of diffusing Te atoms. With no pre-annealing, the number of surface trapping sites (Fig. 4.3f)) is at a minimum. The potential for an atom to be bound to a trapping site is low, and the average desorption rate of the deposited Te atoms is maximized. Pre-annealing leads to the production of Se vacancies in substrate[68–71], and DFT predicts that these will trap a Te atom with a binding energy of 4.9 eV. Thus, one expects that the vacancies will become substitutional Te defects. The substrate Te substitutional defects then act as a trapping site for additional Te atoms. DFT predicts that this binding energy is 1.6 eV, which is greater than that computed for a Te atom binding in a pristine substrate by 95 meV. So, on average, a Te atom has a longer residence time on the substrate for a pre-annealed sample.

The nucleation rate of clusters is probably a combination of heterogeneous and homogeneous nucleation. Consider the growth morphologies of Fig. 4.2a)–c). Clearly, pre-annealing at 200 °C leads to a higher nucleation rate than that without pre-annealing. This is most likely due to heterogeneous nucleation (Fig. 4.3f)). However, it appears that as the pre-annealing temperature is increased to 300 °C, the nucleation rate decreases. A possible explanation for this is that the vacancies produced in the substrate begin to cluster. DFT predicts that the Se divacancy in WSe_2 is bound by 105 meV. If true, as the vacancies form, the number of clusters depends on the ratio of the diffusion coefficient to the rate of production of vacancies [72]. If this ratio increases rapidly with temperature, then the number of clusters in the 300 °C pre-annealing case will be reduced relative to the 200 °C pre-annealing treatment, and the heterogeneous nucleation rate will be, accordingly, decreased.

Once the clusters are nucleated, they grow through the aggregation of atoms, both from the vapor and from the surface. Occasionally, if two atoms bound to the edge of a wire encounter one another, they can nucleate and adjacent wire, and the width of the flake increases. Alternatively, a Te atom diffusing along the edge of a wire may encounter and bind to a Te substitutional defect in the substrate. This bound atom would start a new chain that would align with the original. In this manner, the growing needles can expand to become a film.

The orientation of the wires (armchair vs zigzag) are determined by both kinetics and thermodynamics. Though the films are not strongly bound to the substrate, the symmetry of the substrate clearly impacts the growth morphology. Empirically, the chains aligned along the armchair direction seemed favored, but it is difficult to assess the relative binding energies of the two configurations using DFT because the size of the cells necessary to obtaining a low stress configuration are prohibitive.

The crucial role of substrate interaction in the orientation on Te chains was further checked experimentally. Te was grown on MoS_2, $MoSe_2$, and WS_2, all similar three-fold symmetric substrates, using a substrate pre-annealing at 300 °C and growth at 100 °C. While the sizes of the Te flakes varied, all of them exhibited the same orientation of the Te chains along one of the substrate's three high-symmetry directions.

Furthermore, to achieve single-crystal-like flake growth, Te was grown at 130 °C on a WTe_2 pre-annealed at 300 °C substrates. As WTe_2 has a two-fold rotation axis, we expect all the chains to be aligned in the same direction. Indeed, electron backscatter diffraction (EBSD) was performed on the Te/WTe_2 structure to determine its crystallinity and growth orientation, indicating single-crystal-like texture of the grown Te on the WTe_2 surface. C-axis of Te is aligned perpendicularly to the a-axis of WTe_2 (tungsten atomic chains), and (10-10) planes are paralleled to the surface based on the EBSD results.

4.2 Conclusions

We realized oriented growth of ultrathin Te on 2D surfaces via van der Waals epitaxy on WSe_2, WS_2, $MoSe_2$, MoS_2, and WTe_2 flakes. DFT was used to model the growth behavior of the Te atoms, and a plausible explanation for the increased surface coverage in the case of a pre-annealed substrate was offered. Finally, using a pre-annealed substrate, we achieved the growth of single-crystal textured Te on WTe_2.

Chapter 5

Conclusions and future work

Throughout this thesis, I have presented models that, relying on basic science, explain complex phenomena that occur during semiconductor manufacturing. Chapter 2 presents a model of the SEMD method. The model offers a quantitative selectivity criteria to determine whether the SEMD method will work for a specific system based on the liquid contact angle and the nature (compressive or tensile) strain of the film; this criteria is summarized in Fig. 2.7. Even though Ref. [8] reports the synthesis of WSe_2 monolayer with both tensile and compressive strain, the selectivity criteria remains to be tested experimentally. Further experiments may involve growing monolayers on substrates patterned with materials with different thermal coefficients of expansion, ideally ones predicted to result in widely different elastic states of the film (like silica and strontium titanate for WSe_2 [8]), and explore the effects of SEMD. Another way to create interesting elastic state patterns is to "weld" the film to the substrate by putting islands of other materials with stronger interaction to the substrate on top of it.

Some theoretical advances can also be made to the SEMD model. As is, the model can only manage circular, concentric shapes, and any departure from this results in a very complex system of differential equations. However, it may be possible to, using the same physical assumptions presented in this work, develop a finite-element method that is capable of computing the resulting elastic state of systems with complex geometries. While it is predicted that the necessary forces for maintaining the initial stress on the film need not to be large, and can be sustained the van der Waals bonds with the substrate, there is also evidence [13] that the combination of these bonds along with the thermal vibrations might result in some very interesting strain maps at the atomic scale. The maps show vortex-like atomic displacements, resulting in a metastable equilibrium state where strain is present; the effect of the droplet will then be to "kick" the system out of this state into the global energy minimum, releasing thus the strain.

Chapter 3 uses classical nucleation theory to develop an understanding of the amorphous-to-crystal transition in vapor grown Te thin films. Because of the anisotropic nature of Te properties, large areas of single crystal Te are desired. It was seen experimentally, and later confirmed by the model, that decreasing the temperature inhibited the nucleation, therefore

resulting an larger average crystal area; the downside of this is that a lower temperature also means slower growth, rendering the method a poor candidate for industrial scaling. A way to overcome this would be suppress the homogeneous nucleation by engineering the substrate to make the Te impingement rate as low as possible (how can this be done is a problem for future engineers), and rely only on heterogeneous nucleation starting at the edges of the substrate or at impurities and defects. With such a system, it may be possible to have a low nucleation rate that does not depend on temperature and a decent growth rate.

Lastly, the growth of oriented Te films was explored in chapter 4. The chapter outlined the importance of the substrate pre-annealing treatment, which greatly increases the impingement Te rate. In this case, however, having a good impingement rate might be desirable, as the direction of the Te chains can be determined by the substrate. While it is empirically know that thermal treatment leads to vacancies on the substrates used in this work, the theoretical study does not get beyond saying that this vacancies enhance the impingement rate, and currently the underlying mechanism is not know.

Bibliography

[1] Richard Nock and Frank Nielsen. Statistical region merging. *IEEE Transactions on Pattern Analysis and Machine Intelligence*, 26(11):1452–1458, 2004.

[2] Sheneve Z. Butler, Shawna M. Hollen, Linyou Cao, Yi Cui, Jay A. Gupta, Humberto R. Gutiérrez, Tony F. Heinz, Seung Sae Hong, Jiaxing Huang, Ariel F. Ismach, Ezekiel Johnston-Halperin, Masaru Kuno, Vladimir V. Plashnitsa, Richard D. Robinson, Rodney S. Ruoff, Sayeef Salahuddin, Jie Shan, Li Shi, Michael G. Spencer, Mauricio Terrones, Wolfgang Windl, and Joshua E. Goldberger. Progress, challenges, and opportunities in two-dimensional materials beyond graphene. *ACS Nano*, 7(4):2898–2926, 2013.

[3] Qing Hua Wang, Kourosh Kalantar-Zadeh, Andras Kis, Jonathan N. Coleman, and Michael S. Strano. Electronics and optoelectronics of two-dimensional transition metal dichalcogenides. *Nature Nanotechnology*, 7(11):699–712, 2012.

[4] Rafael Roldán, Andrés Castellanos-Gomez, Emmanuele Cappelluti, and Francisco Guinea. Strain engineering in semiconducting two-dimensional crystals. *Journal of Physics Condensed Matter*, 27(31), 2015.

[5] Hiram J. Conley, Bin Wang, Jed I. Ziegler, Richard F. Haglund, Sokrates T. Pantelides, and Kirill I. Bolotin. Bandgap engineering of strained monolayer and bilayer MoS2. *Nano Letters*, 13(8):3626–3630, 2013.

[6] Yeung Yu Hui, Xiaofei Liu, Wenjing Jie, Ngai Yui Chan, Jianhua Hao, Yu Te Hsu, Lain Jong Li, Wanlin Guo, and Shu Ping Lau. Exceptional tunability of band energy in a compressively strained trilayer MoS2 sheet. *ACS Nano*, 7(8):7126–7131, 2013.

[7] Sujay B. Desai, Gyungseon Seol, Jeong Seuk Kang, Hui Fang, Corsin Battaglia, Rehan Kapadia, Joel W. Ager, Jing Guo, and Ali Javey. Strain-induced indirect to direct bandgap transition in multilayer WSe2. *Nano Letters*, 14(8):4592–4597, 2014.

[8] Geun Ho Ahn, Matin Amani, Haider Rasool, Der Hsien Lien, James P. Mastandrea, Joel W. Ager, Madan Dubey, Daryl C. Chrzan, Andrew M. Minor, and Ali Javey. Strain-engineered growth of two-dimensional materials. *Nature Communications*, 8(1):1–7, 2017.

[9] Hyungjin Kim, Geun Ho Ahn, Joy Cho, Matin Amani, James P Mastandrea, Catherine K Groschner, Der-hsien Lien, Yingbo Zhao, Joel W. Ager, Mary C Scott, Daryl C Chrzan, and Ali Javey. Synthetic WSe 2 monolayers with high photoluminescence quantum yield. *Science Advances*, 5(1):eaau4728, 2019.

[10] H. Batiz, Ji Guo, Geun Ho Ahn, Hyungjin Kim, Ali Javey, J. W. Ager, and D. C. Chrzan. Theory of liquid-mediated strain release in two-dimensional materials. *Physical Review Materials*, 6(5):1–10, 2022.

[11] Vladimir Ivanovich Smirnov. *A Course of Higher Mathematics: Vol. 4, Integral Equations and Partial Differential Equations*. Pergamon Press, 1964.

[12] Michel Grandbois, Martin Beyer, Matthias Rief, Hauke Clausen-Schaumann, and Hermann E. Gaub. How strong is a covalent bond? *Science*, 283(5408):1727–1730, 1999.

[13] Ji Guo, H. Batiz, and D. C. Chrzan. Unpublished research. 2021.

[14] Deniz ÇakIr, François M. Peeters, and Cem Sevik. Mechanical and thermal properties of h -MX2(M = Cr, Mo, W; X = O, S, Se, Te) monolayers: A comparative study. *Applied Physics Letters*, 104(20), 2014.

[15] Meenakshi Annamalai, Kalon Gopinadhan, Sang A. Han, Surajit Saha, Hye Jeong Park, Eun Bi Cho, Brijesh Kumar, Abhijeet Patra, Sang Woo Kim, and T. Venkatesan. Surface energy and wettability of van der Waals structures. *Nanoscale*, 8(10):5764–5770, 2016.

[16] Joseph J. Jasper. The Surface Tension of Pure Liquid Compounds. *Journal of Physical and Chemical Reference Data*, 1(4):841–1010, 1972.

[17] R. Kern and P. Müller. Deformation of an elastic thin solid induced by a liquid droplet. *Surface Science*, 264(3):467–494, 1992.

[18] Lee R. White. The contact angle on an elastic substrate. 1. The role of disjoining pressure in the surface mechanics. *Journal of Colloid and Interface Science*, 258(1):82–96, 2003.

[19] Elizabeth R. Jerison, Ye Xu, Larry A. Wilen, and Eric R. Dufresne. Deformation of an elastic substrate by a three-phase contact line. *Physical Review Letters*, 106(18):1–4, 2011.

[20] Ying Song Yu. Circular plate deformed by a sessile droplet. *Journal of Adhesion Science and Technology*, 28(19):1970–1979, 2014.

[21] Soon Hong Yuk and Mu Shik Jhon. Contact angles on deformable solids. *Journal of Colloid And Interface Science*, 110(1):252–257, 1986.

[22] Didier Long, Armand Ajdari, and Ludwik Leibler. Static and dynamic wetting properties of thin rubber films. *Langmuir*, 12(21):5221–5230, 1996.

[23] Ying Song Yu. Substrate elastic deformation due to vertical component of liquid-vapor interfacial tension. *Applied Mathematics and Mechanics (English Edition)*, 33(9):1095–1114, 2012.

[24] Heyi Liang, Zhen Cao, Zilu Wang, and Andrey V. Dobrynin. Surface Stresses and a Force Balance at a Contact Line. *Langmuir*, 34(25):7497–7502, 2018.

[25] Zhen Cao and Andrey V. Dobrynin. Polymeric droplets on soft surfaces: From Neumann's triangle to Young's law. *Macromolecules*, 48(2):443–451, 2015.

[26] Martin E.R. Shanahan. Contact Angle Equilibrium on Thin Elastic Solids. *The Journal of Adhesion*, 18(4):247–267, 1985.

[27] M. E.R. Shanahan. The influence of solid micro-deformation on contact angle equilibrium. *Journal of Physics D: Applied Physics*, 20(7):945–950, 1987.

[28] Martin E.R. Shanahan. Equilibrium of liquid drops on thin plates; plate rigidity and stability considerations. *The Journal of Adhesion*, 20(4):261–274, 1987.

[29] G. Kresse and J. Hafner. Ab initio molecular dynamics for liquid metals. *Physical Review B*, 47(1):558–561, 1993.

[30] G. Kresse and J. Furthmüller. Efficient iterative schemes for ab initio total-energy calculations using a plane-wave basis set. *Physical Review B - Condensed Matter and Materials Physics*, 54(16):11169–11186, 1996.

[31] G. Kresse and J. Furthmüller. Efficiency of ab-initio total energy calculations for metals and semiconductors using a plane-wave basis set. *Computational Materials Science*, 6(1):15–50, 1996.

[32] P. E. Blöchl. Projector augmented-wave method. *Physical Review B*, 50(24):17953–17979, 1994.

[33] John P. Perdew, Kieron Burke, and Matthias Ernzerhof. Generalized gradient approximation made simple. *Physical Review Letters*, 77(18):3865–3868, 1996.

[34] Oleksandr I. Malyi, Vadym V. Kulish, and Clas Persson. In search of new reconstructions of (001) α-quartz surface: A first principles study. *RSC Advances*, 4(98):55599–55603, 2014.

[35] Kang Lai, Wei Bing Zhang, Fa Zhou, Fan Zeng, and Bi Yu Tang. Bending rigidity of transition metal dichalcogenide monolayers from first-principles. *Journal of Physics D: Applied Physics*, 49(18), 2016.

[36] Daniel S Fisher. Sliding charge-density waves as a dynamic critical phenomenon. *Physical Review B*, 31(3):1396, 1985.

[37] Jean M Carlson, James S Langer, and Bruce E Shaw. Dynamics of earthquake faults. *Reviews of Modern Physics*, 66(2):657, 1994.

[38] D. C. Chrzan and MJ Mills. Criticality in the plastic deformation of ni_3al. *Physical review letters*, 69(19):2795, 1992.

[39] D. C. Chrzan and M. J. Mills. Criticality in the plastic deformation of l_{12} intermetallic compounds. *Physical Review B*, 50(1):30, 1994.

[40] D. C. Chrzan and Murray S Daw. Pinning-depinning transition in dislocation dynamics. *Physical Review B*, 55(2):798, 1997.

[41] Zhiwei Peng, Xiaolin Chen, Yulong Fan, David J. Srolovitz, and Dangyuan Lei. Strain engineering of 2D semiconductors and graphene: from strain fields to band-structure tuning and photonic applications. *Light: Science and Applications*, 9(1), 2020.

[42] Motoyasu Terao, Kazuo Shigematsu, Masahiro Ojima, Yoshio Taniguchi, Shinkichi Horigome, and Seiji Yonezawa. Chalcogenide thin films for laser-beam recordings by thermal creation of holes. *Journal of Applied Physics*, 50(11):6881–6886, 1979.

[43] Motoyasu Terao, Shinkichi Horigome, and Kazuo Shigematsu. Resistance To Oxidation Of Te-Se Optical Recording Films. *Proceedings of SPIE*, 382(January 1983), 1983.

[44] P. Kivits, B. Jacobs, and P. Zalm. Summary Abstract: Research on materials for optical storage. *Journal of Vacuum Science and Technology*, 18(1):68–69, 1981.

[45] P. Kivits, R. De Bont, B. Jacobs, and P. Zalm. The hole formation process in tellurium layers for optical data storage. *Thin Solid Films*, 87(3):215–231, 1982.

[46] Chunsong Zhao, Chaoliang Tan, Der Hsien Lien, Xiaohui Song, Matin Amani, Mark Hettick, Hnin Yin Yin Nyein, Zhen Yuan, Lu Li, Mary C. Scott, and Ali Javey. Evaporated tellurium thin films for p-type field-effect transistors and circuits. *Nature Nanotechnology*, 15(1):53–58, 2020.

[47] Taikyu Kim, Cheol Hee Choi, Pilgyu Byeon, Miso Lee, Aeran Song, Kwun Bum Chung, Seungwu Han, Sung Yoon Chung, Kwon Shik Park, and Jae Kyeong Jeong. Growth of high-quality semiconducting tellurium films for high-performance p-channel field-effect transistors with wafer-scale uniformity. *npj 2D Materials and Applications*, 6(1):1–7, 2022.

[48] Muhammad Naqi, Kyung Hwan Choi, Hocheon Yoo, Sudong Chae, Bum Jun Kim, Seungbae Oh, Jiho Jeon, Cong Wang, Na Liu, Sunkook Kim, and Jae Young Choi. Nanonet: Low-temperature-processed tellurium nanowire network for scalable p-type field-effect transistors and a highly sensitive phototransistor array. *NPG Asia Materials*, 13(1), 2021.

[49] Gang Qiu, Adam Charnas, Chang Niu, Yixiu Wang, Wenzhuo Wu, and Peide D. Ye. The resurrection of tellurium as an elemental two-dimensional semiconductor. *npj 2D Materials and Applications*, 6(1):1–10, 2022.

[50] Chunsong Zhao, Humberto Batiz, Bengisu Yasar, Hyungjin Kim, Wenbo Ji, Mary C Scott, Daryl C Chrzan, and Ali Javey. Tellurium Single-Crystal Arrays by Low-Temperature Evaporation and Crystallization. *Advanced Materials*, 33(37):1–9, 2021.

[51] A. A. Abu-Sehly, M. Rashad, M. M. Hafiz, A. A.L. Abd-Elmageed, and R. Amin. Tuning optical properties of thin films based on selenium tellurium. *Optical Materials*, 109(August):110291, 2020.

[52] Zhe Shi, Rui Cao, Karim Khan, Ayesha Khan Tareen, Xiaosong Liu, Weiyuan Liang, Ye Zhang, Chunyang Ma, Zhinan Guo, Xiaoling Luo, and Han Zhang. Two-Dimensional Tellurium: Progress, Challenges, and Prospects. *Nano-Micro Letters*, 12(1):1–34, 2020.

[53] Seho Yi, Zhili Zhu, Xiaolin Cai, Yu Jia, and Jun Hyung Cho. The Nature of Bonding in Bulk Tellurium Composed of One-Dimensional Helical Chains. *Inorganic Chemistry*, 57(9):5083–5088, 2018.

[54] Robert W. Dutton and Richard S. Muller. Electrical properties of tellurium thin films. *Proceedings of the IEEE*, 59(10):1511–1517, 1971.

[55] Katsuro Okuyama and Yasuji Kumagai. Grain growth of evaporated Te films on a heated and cooled substrate. *Journal of Applied Physics*, 46(4):1473–1477, 1975.

[56] Alexis de Vos and Jan Aerts. The influence of deposition rate on the electrical properties of thin tellurium films. *Thin Solid Films*, 46(2):223–228, 1977.

[57] William A. Johnson and Robert F. Mehl. Reaction Kinetics in Processes of Nucleation and Growth. *Transactions of the American Institute of Mining and Metallurgical Engineers*, 135:416–442, 1939.

[58] Melvin Avrami. Kinetics of Phase Change. I General Theory. *Journal of Chemical Physics*, 7:1103–1112, 1939.

[59] A. N. Kolmogorov. On the statistical theory of metal crystallization (1937). In *Selected works of AN Kolmogorov*, volume 2, pages 188–192. 1991.

[60] Katayun Barmak. A Commentary on: "Reaction Kinetics in Processes of Nucleation and Growth". *Metallurgical and Materials Transactions B*, 49(6):3616–3680, 2018.

[61] V. I. Kalikmanov. *Nucleation Theory*. Springer, Dordrecht, 2013.

[62] Johannes Schindelin, Ignacio Arganda-Carreras, Erwin Frise, Verena Kaynig, Mark Longair, Tobias Pietzsch, Stephan Preibisch, Curtis Rueden, Stephan Saalfeld, Benjamin Schmid, Jean Yves Tinevez, Daniel James White, Volker Hartenstein, Kevin Eliceiri, Pavel Tomancak, and Albert Cardona. Fiji: An open-source platform for biological-image analysis. *Nature Methods*, 9(7):676–682, 2012.

[63] Wolfram Research, Inc. Mathematica, Version 13.0.0. Champaign, IL, 2021.

[64] Anubhav Jain, Shyue Ping Ong, Geoffroy Hautier, Wei Chen, William Davidson Richards, Stephen Dacek, Shreyas Cholia, Dan Gunter, David Skinner, Gerbrand Ceder, and Kristin A. Persson. Commentary: The materials project: A materials genome approach to accelerating materials innovation. *APL Materials*, 1(1), 2013.

[65] Norman A. Blum and Charles Feldman. The Crystallization of Amorphous Germanium Films. *Journal of Non*, 22(1):29–35, 1976.

[66] Chunsong Zhao, Humberto Batiz, Bengisu Yasar, Wenbo Ji, Mary C. Scott, Daryl C. Chrzan, and Ali Javey. Orientated Growth of Ultrathin Tellurium by van der Waals Epitaxy. *Advanced Materials Interfaces*, 2101540:2101540, 2022.

[67] Bales. G.S and Zangwill. A. Morphological instability of a terrace edge during step flow growth. *Physical Review B*, 41(V):5500–5508, 1990.

[68] M. Donarelli, F. Bisti, F. Perrozzi, and L. Ottaviano. Tunable sulfur desorption in exfoliated MoSby means of thermal annealing in ultra-high vacuum. *Chemical Physics Letters*, 588:198–202, 2013.

[69] William H. Blades, Nicholas J. Frady, Peter M. Litwin, Stephen J. Mcdonnell, and Petra Reinke. Thermally Induced Defects on WSe2. *Journal of Physical Chemistry C*, 124(28):15337–15346, 2020.

[70] Ying Sun, Xuewei Zhang, Baoguang Mao, and Minhua Cao. Controllable selenium vacancy engineering in basal planes of mechanically exfoliated WSe2 monolayer nanosheets for efficient electrocatalytic hydrogen evolution. *Chemical Communications*, 52(99):14266–14269, 2016.

[71] Sefaattin Tongay, Joonki Suh, Can Ataca, Wen Fan, Alexander Luce, Jeong Seuk Kang, Jonathan Liu, Changhyun Ko, Rajamani Raghunathanan, Jian Zhou, Frank Ogletree, Jingbo Li, Jeffrey C. Grossman, and Junqiao Wu. Defects activated photoluminescence in two-dimensional semiconductors: Interplay between bound, charged, and free excitons. *Scientific Reports*, 3:1–5, 2013.

[72] G. S. Bales and D. C. Chrzan. Dynamics of irreversible island growth during submonolayer epitaxy. *Physical Review B*, 50(9):6057–6067, 1994.